The Aeronautical Journal (2026), 1–27
doi:10.1017/aer.2026.10132

RESEARCH ARTICLE

Nonlinear adaptive longitudinal controller and flight qualities validation for a business aircraft

R. P. Andrianantara, G. Ghazi and R. M. Botez

Laboratory of Applied Research in Active Controls, Avionics and AeroServoElasticity (LARCASE), System Engineering Department, École de technologie supérieure (ÉTS), Montreal, Canada
Corresponding author: R. M. Botez; Email: ruxandra@gpa.etsmtl.ca

Received: 26 February 2025; **Revised:** 2 January 2026; **Accepted:** 6 January 2026

Keywords: adaptive control; flight control; nonlinear control; online state estimation; RLS

Abstract

This paper presents the design of a nonlinear adaptive flight control system for the Cessna Citation X longitudinal dynamics. The aircraft pitch rate is controlled using a combination of recursive least squares-based nonlinear dynamic inversion and an adaptive neural network controller. The recursive least squares algorithm provides online parameter estimates to support the inversion, while the neural network compensates for residual modeling errors through online weight adaptation. To enhance robustness and ensure stability, a fixed-gain proportional integral derivative controller is integrated into the control structure. Unlike conventional gain-scheduled controllers, where PID gains vary with flight condition, the proposed adaptive controller uses a single baseline set of fixed gains. The adaptive component updates the control action online, enabling the same controller configuration to operate effectively across all 64 cruise conditions without any gain scheduling. A systematic tuning methodology is introduced for initialising the recursive least squares, selecting forgetting factors and applying covariance resets to ensure accurate adaptation. The controller is able to track a pitch-rate reference model that satisfies longitudinal flight quality requirements. Robustness is assessed under realistic disturbances, including wind gusts, Dryden turbulence, actuator loss-of-effectiveness and actuator noise. Simulation results demonstrate that the controller achieves precise reference tracking while maintaining Level 1 flight qualities. Stability is formally guaranteed using Lyapunov-based analysis. The findings highlight the ability of the designed hybrid adaptive controller to overcome limitations of linearisation, gain scheduling and estimator sensitivity, forecasting a practical and certifiable method for the integration of intelligent adaptive flight control systems into commercial aircraft.

Nomenclature

T_{θ_2}	short period time constant
x_{cg}	centre of gravity
CAP	control anticipation parameter
CAS	calibrated airspeed
CoG	centre of gravity
DI	dynamic inversion
f, g	unknown nonlinear functions
FQ	flight quality
ICAO	International Civil Aviation Organization
LOC-II	loss-of-control in flight
LOE	loss-of-effectiveness
NDI	nonlinear dynamic inversion
NN	neural network
PID	proportional integral derivative
RAFS	research aircraft flight simulator

RLS	recursive least square
$\mathbf{F}$, $\hat{\mathbf{F}}$	local state matrix and its estimate, respectively
$\mathbf{G}$, $\hat{\mathbf{G}}$	local control matrix and its estimates, respectively
$\mathbf{I}$	unit matrix
$\mathbf{L}$	covariance matrix
$\mathbf{V}$, $\mathbf{W}$	neural network weight matrices
m	mass
q	pitch rate
u, v, w	velocity components

Greek symbol

δ_e	elevator deflection
ξ_{sp}	short period damping
ω_{sp}	short period natural frequency
$\mathbf{\Delta} t$	time step
$\mathbf{\Gamma}$	learning rate matrix
$\mathbf{\Theta}$, $\hat{\mathbf{\Theta}}$	matrix of unknown parameters and its estimate
θ	pitch angle
κ	forgetting factor
λ	scalar
σ, σ'	sigmoid transfer function and its gradient
$\boldsymbol{\varphi}$	unknown nonlinear function
ϵ	RLS estimation error

1.0 Introduction

Flight control systems are critical for maintaining stability and safety in aircraft operations. According to the Federal Administration Aviation (FAA), human errors contribute to nearly 60% to 80% of aircraft accidents [1], which are often due to unmitigated environmental hazards or system failures. Advanced flight control laws therefore play a central role in reducing pilot workload, enhancing autonomy and improving operational safety. Compared to costly structural modifications, software-based enhancements at the control level, such as flutter suppression or manoeuvre load alleviation, provide more flexible and efficient solutions [2]. This motivates the development of adaptive and intelligent controllers that can reliably handle uncertainties in real time.

Traditional flight control architectures still primarily rely on linear controllers such as proportional integral derivative (PID) and linear quadratic regulator (LQR) designs [3]. These methods are straightforward and well-established offering proven stability with guaranteed gain and phase margins. However, they require precise gain scheduling [4] to ensure adequate performance across the aircraft's full envelope and under varying operating conditions. The tuning of these controllers is based on linearised models, which often neglect higher-order nonlinearities [3]. Consequently, performance degrades and stability margins may deteriorate when the aircraft operates outside the scheduled regime. Robust control techniques such as H_∞ [5, 6] and linear quadratic Gaussian (LQG) controllers [7] mitigate certain uncertainties, but they are still strongly dependent on accurate mathematical models.

Advanced nonlinear control methods, such as nonlinear dynamic inversion (NDI) [8–10] and model predictive control (MPC) [11], address several of the limitations of traditional linear techniques. However, both approaches depend heavily on precise state-space models [12–14], making them sensitive to parameter variations, unmodeled dynamics or environmental disturbances. This reliance on precise linearisation remains one of the main obstacles to their widespread application in commercial aircraft.

To mitigate this dependence, online estimation techniques such as recursive least squares (RLS) [15–17] and extended Kalman filtering (EKF) [18] have been developed, enabling incremental model updates [19] and adaptive compensation of the dynamic inversion [20–22] or MPC controllers [23]. Although effective in principle, their performance is often sensitive to initialisation conditions, forgetting factor selection, and numerical instabilities, which can compromise real-time implementation.

In parallel, intelligent control approaches have demonstrated the ability of neural networks [24–26], fuzzy logic [27–29] and hybrid adaptive controllers [30–32] to capture nonlinearity and compensate for unmodeled dynamics. Robust adaptive control, in particular, has raised interests due to its effectiveness in compensating for time-varying dynamics and in controlling highly nonlinear systems, including actuator dynamics [10].

Foundational works by Ref. [22] introduced hybrid adaptive control architectures that combines baseline inversion controllers, indirect parameter estimation using RLS and adaptive neural networks adaptive controllers for compensation [22–33]. These studies validated the hybrid concept for damaged aircraft and launch vehicles [34]. More recent applications on the Cessna Citation X [20–23] have demonstrated the potential of dynamic inversion combined with neural network controllers. However, while these studies established the foundation for hybrid adaptive dynamic inversion, their scope was limited in terms of flight conditions and did not address certification-level validation. This study extends their findings by systematically analysing RLS estimation sensitivity, integrating neural networks adaptive learning and demonstrating Level 1 flight qualities under FAA standards.

This paper advances the state of the art by implementing a hybrid RLS – NN adaptive controller for the longitudinal pitch-rate control of the Cessna Citation X. Unlike prior studies, the controller is designed and validated across 64 flight conditions covering the aircraft cruise envelope, thereby removing the need to gain scheduling. In this architecture, the baseline PID controller operates with fixed gains to provide stability, while only the RLS estimator and NN residual compensator adapt online. This design eliminates the need for repeated across conditions, as adaptation is handled automatically by the adaptive controllers. Furthermore, this study provides a systematic analysis of RLS adaptation mechanisms, including initialisation, forgetting factors and covariance resets, and evaluates their impact on both stability and accuracy. Neural networks are then integrated for direct control, providing robust adaptation even in case of degraded RLS estimates. Importantly, flight qualities are explicitly validated, showing Level 1 compliance [35–37], while nonlinear stability is formally guaranteed through Lyapunov-based analysis [38, 39].

Related controller structures with different compensation strategies have been assessed by other researchers. Steffensen et al. [10] examined nonlinear dynamic inversion (DI) with incremental control perspectives, including first-order actuator dynamics, showing improved robustness but without NN augmentation nor analysis of wide-range uncertainties. Harris et al. [12] applied L1 adaptive DI ensuring fast adaptation but with a strong dependence on accurate modelling and without formal flight quality assessment. More recently, Andrianantara et al. [23] extended their earlier study by combining MPC with RLS and NN augmentation for the Cessna Citation X, demonstrating performance gains but without systematic RLS estimator tuning or robustness validation. In contrast, the present study incorporates higher-order actuator dynamics, introduces a formal tuning methodology and conducts comprehensive robustness testing. Taken together, these contributions help bridge the gap between theoretical adaptive controller designs and certifiable implementations suitable for commercial aircraft.

Several researchers have focused their efforts on unmanned aerial vehicle (UAV) applications, where agility and adaptability are prioritised over certifiability. This is made possible due to the fact that UAVs present less risk to human life, as being remotely controlled. O'Connell et al. [40] demonstrated rapid NN-based adaptation for UAV flight in strong winds, but relied primarily on reinforcement learning without model-based stability guarantees. Zhou et al. [41] proposed extended incremental DI with optical-flow feedback for micro air vehicles, confirming feasibility but only in small-scale systems. Earlier, Pedro and Meyer [30] applied NN-based DI to fighter aircraft, showing improved nonlinear tracking in simulations but without robustness validation. Similarly, Lungu and Lungu [31] applied NN – DI to landing autopilots, enhancing robustness during approach and flare, while

Table 1. *Cessna Citation X flight specifications*

Characteristics	Value
Maximum cruise speed	648 km/h [350 kn]
Maximum Mach number	0.92
Maximum range	5, 724 km [3,091 nm]
Maximum altitude	15,544 m [51,000 ft]
Maximum takeoff weight	16,193 kg [35,700 lb]
Maximum zero fuel weight	11,067 kg [24,400 lb]
Maximum thrust	28,655 N [6442 lbf]

Lungu et al. [32] later extended NN – DI concepts to spacecraft control. These studies confirm the adaptability of NN-augmented DI across various domains; however, they are limited to UAV-scale or highly specific applications. This study, instead, focuses on manned commercial aircraft, for which a high-fidelity research aircraft flight simulator is available, thereby extending NN – DI hybrid approaches into a certifiable, envelope-wide framework.

In summary, the benefits of the proposed controller are twofold. First, the architecture is simplified, since gain-scheduled controllers are replaced by a single adaptive configuration capable of covering the entire cruise envelope. Second, the controller demonstrates robustness against a wide range of uncertainties, including turbulence, actuator loss-of-effectiveness and actuator noise, while maintaining compliance with flight quality requirements.

By addressing long-standing limitations related to gain scheduling, model dependence and estimator sensitivity, this work provides a practical and certifiable method for integrating intelligent adaptive controllers into commercial aircraft. While previous studies [10–12] have validated adaptive NN – DI concepts in specific operating conditions, UAVs, or specialised mission phases, this study systematically assesses 64 cruise conditions of the Cessna Citation X, integrates NN residual learning with RLS sensitivity analysis, incorporates higher-order actuator dynamics and validates flight qualities against FAA Level 1 standards. This represents a significant step beyond feasibility demonstrations and aligns with ongoing certification initiatives from the FAA, EASA and NASA [42–44], thereby reinforcing both the relevance and applicability of the proposed approach.

The remainder of this paper is organised as follows: Section 2 presents the methodology and controller design; Section 3 details the tuning strategy and results for ideal conditions; Section 4 provides robustness evaluation; Section 5 discusses findings; and Section 6 concludes with final remarks. The Lyapunov stability assessment is provided in the appendix.

1.1 Aircraft model and simulation platform

1.1.1 Cessna Citation X aircraft specifications

The Cessna Citation X is a long-range business jet that has been widely used as a platform for advanced control design [23–29]. Since its introduction in 1996, the business jet aircraft has been recognised as one of the fastest business jets ever produced, with a maximum cruise speed of 350 kn and a maximum Mach number of 0.92. The aircraft is powered by two Rolls-Royce AE3007C-1 turbofan engines, each providing a maximum thrust of 28,655 N. Its cabin accommodates up to 12 passengers and three crew members.

The Cessna Citation X has a maximum range of 5,724 km and a service ceiling of 15,544 m. Its main performance characteristics, summarised in Table 1, make the Cessna Citation X an excellent candidate for adaptive control studies. In fact, its wide and available operational envelope, high performance and high-fidelity simulation models [45] provide a realistic platform for evaluating adaptive flight control architectures.

Figure 1. *Cessna Citation X research aircraft flight simulator (RAFS) manufactured by CAE Inc.*

1.1.2 Nonlinear Simulink platform

A high-fidelity nonlinear model of the Cessna Citation X was developed in MATLAB/Simulink [45] and serves as a research platform for the controller design. This Simulink model integrates several modules such as aerodynamics, engine dynamics, actuator and sensor dynamics, atmospheric disturbance effects and other relevant aircraft systems.

The Simulink model was cross-validated using simulated flight data from a Research Aircraft Flight Simulator (RAFS) of the Cessna Citation X, designed and manufactured by CAE Inc. [45] and shown in Fig. 1. The RAFS has been validated by CAE engineers, based on qualification test guide (QTG) procedures and real flight-test data from the Cessna Citation X. In addition, the RAFS satisfies the flight simulator validation criteria imposed by the Federal Aviation Administration (FAA) and can be considered comparable to Level D fidelity with respect to flight dynamics. The flight dynamics implemented within the RAFS are based on CAE Inc. and Cessna Aircraft (Textron) proprietary data and are therefore not publicly accessible. However, the RAFS provides access to high-fidelity simulated flight data and supports the execution of a wide range of flight scenarios, manoeuvres and full-mission simulations. The MATLAB/Simulink environment was developed to reproduce the RAFS flight dynamics with sufficient accuracy to support advanced control design, thereby ensuring that controller development and evaluation are conducted on high-fidelity flight dynamics.

In addition, the Cessna Citation X simulation platforms, both the RAFS and the derived Simulink models, have been widely used in advanced control research and peer-reviewed research literature. Examples of application include NN-based adaptive controllers with approximate dynamic inversion [20, 21] and model predictive controllers [14]. Similarly, fuzzy logic and recurrent neural network controllers have been demonstrated for longitudinal and lateral control [29–51], while control clearance and lateral flight qualities were investigated in [49, 50].

Table 2. *Actuator dynamics parameter*

Parameter	Value
Natural frequency	20 rad/s
Maximum deflection	14°
Minimum deflection	−19°
Damping ratio	0.8
Rate limit	20°/sec

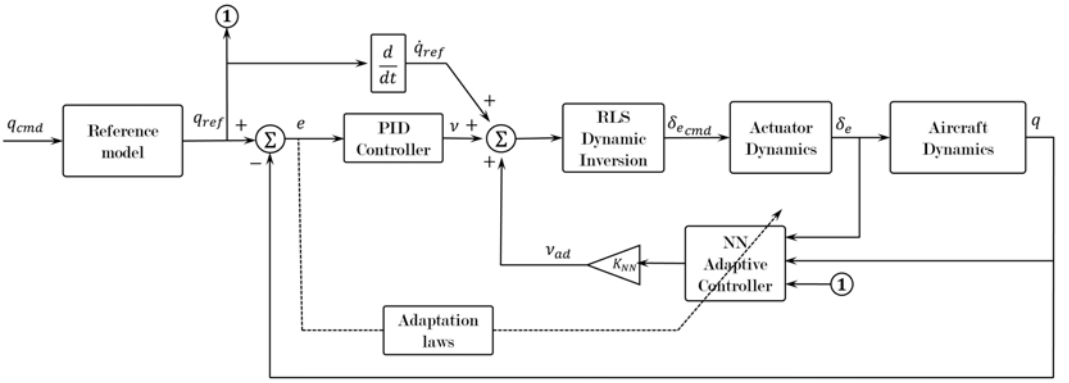

Figure 2. *Pitch rate model reference adaptive controller using PID, RLS dynamic inversion and adaptive NN.*

1.2 Nonlinear dynamic model

1.2.1 Cessna Citation X nonlinear dynamic model

The aircraft's longitudinal dynamics were considered in this study. This assumption allows us to write the following nonlinear representation of the aircraft's longitudinal dynamics:

$$\begin{aligned} \dot{\mathbf{x}} &= \boldsymbol{\varphi}(\mathbf{x}, \eta) \\ y &= h(\mathbf{x}) \end{aligned} \tag{1}$$

where $\mathbf{x} = [u \quad w \quad q \quad \theta]^T$ is the state vector, u and w are the longitudinal and lateral velocity components, respectively, q is the pitch rate θ is the pitch angle, h is a nonlinear function, $\eta = \delta_e$ is the elevator input and $\boldsymbol{\varphi}$ is an unknown nonlinear function.

1.2.2 Nonlinear actuator dynamics

The actuators are modelled in Simulink using a second-order nonlinear transfer function. This allows us to realistically reproduce the higher-order nonlinearity that strongly affect aircraft stability and control performance, particularly in adaptive flight control studies [10]. The actuator parameters are summarised in Table 2.

2.0 Pitch rate controller design

2.1 Controller architecture

Figure 2 presents the controller architecture for the pitch rate control. The control elements include a baseline PID controller, an RLS-based DI controller and a NN adaptive controller. The stability analysis is detailed in the appendix.

Controlling the pitch rate q for longitudinal control aims to track the desired *short period* performances [3]. Therefore, the proposed control algorithm is designed to track a reference signal q_{ref}.

2.2 Controller elements

Nonlinear Dynamic Inversion Controller

For linear systems, DI is straightforward to execute [3]. For nonlinear systems, the inversion is more difficult, as nonlinear systems may include unmodeled dynamics. According to Ref. [3], most aircraft dynamics can be represented in affine form, with respect to the control input. Therefore, Equation (1) can be rewritten as:

$$\begin{aligned} \dot{\mathbf{x}} &= \mathbf{f}(\mathbf{x}) + \mathbf{g}(\mathbf{x})\eta \\ y &= q = \mathbf{C}\mathbf{x} \end{aligned} \tag{2}$$

where f and **g** are nonlinear functions, and y is the output. Hence, C = [0 0 1 0]for pitch rate output.

Inverting Equation (1), the control input may be written as:

$$\eta = \aleph(\dot{\mathbf{x}}, \mathbf{x}) \tag{3}$$

where $\aleph = \boldsymbol{\varphi}^{-1}$ is the inverse function of $\boldsymbol{\varphi}$. Next, let's express $\eta = \delta_e$ according to the control algorithm in Fig. 2. Considering Equations (1) and (2):

$$\dot{\mathbf{x}} = \boldsymbol{\varphi}(\mathbf{x}, \eta) = \mathrm{f}(\mathbf{x}) + \mathbf{g}(\mathbf{x})\eta \tag{4}$$

Developing Equation (4) using the first-order linear approximation around $(\mathbf{x}_0, \eta_0)$, we obtain:

$$\boldsymbol{\varphi}(\mathbf{x}, \eta) = \boldsymbol{\varphi}(\mathbf{x}_0, \eta_0) + \boldsymbol{\varphi}'_x(\mathbf{x}, \eta)_{\mathbf{x}_0,\eta_0}(\mathbf{x} - \mathbf{x}_0) + \boldsymbol{\varphi}'_\eta(\mathbf{x}, \eta)_{\mathbf{x}_0,\eta_0}(\eta - \eta_0) \tag{5}$$

where $\boldsymbol{\varphi}(\mathbf{x}_0, \eta_0)$ is the value at $(\mathbf{x_0}, \eta_0)$, $\boldsymbol{\varphi}'_x(\mathbf{x}, \eta)_{\mathbf{x}_0,\eta_0}$ and $\boldsymbol{\varphi}'_\eta(\mathbf{x}, \eta)_{\mathbf{x}_0,\eta_0}$ are the partial derivatives of $\boldsymbol{\varphi}$ with respect to **x** and η, respectively. We may formulate the terms in Equation (5), such as:

$$\boldsymbol{\varphi}(\mathbf{x}_0, \eta_0) = \mathbf{f}(\mathbf{x}_0) + \mathbf{g}(\mathbf{x}_0)\eta \tag{6.1}$$

$$\boldsymbol{\varphi}'_x(\mathbf{x}, \eta) = \frac{\partial \mathbf{f}(\mathbf{x})}{\partial \mathbf{x}} + \frac{\partial \mathbf{g}(\mathbf{x})}{\partial \mathbf{x}}\eta \tag{6.2}$$

$$\boldsymbol{\varphi}'_\eta(\mathbf{x}, \eta) = \frac{\partial \mathrm{f}(\mathbf{x})}{\partial \eta} + \frac{\partial \left[\mathbf{g}(\mathbf{x})\eta\right]}{\partial \eta} = \mathbf{g}(\mathbf{x}) \tag{6.3}$$

Considering the following changes, so that $\boldsymbol{\Delta}\mathbf{x} = (\mathbf{x} - \mathbf{x}_0)$ and $\boldsymbol{\Delta}\eta = (\eta - \eta_0)$, and substituting Equation (6) into Equation (5), the following expression is obtained:

$$\boldsymbol{\varphi}(\mathbf{x}, \eta) = \mathbf{f}(\mathbf{x}_0) + \mathbf{g}(\mathbf{x}_0)\eta + \left(\frac{\partial \mathbf{f}(\mathbf{x})}{\partial \mathbf{x}} + \frac{\partial \mathbf{g}(\mathbf{x})}{\partial \mathbf{x}}\eta\right)_{\mathbf{x}_0,\eta_0} \Delta\mathbf{x} + \mathbf{g}(\mathbf{x})_{\mathbf{x}_0,\eta_0}\boldsymbol{\Delta}\eta \tag{7}$$

Let us express $\dot{x}$ in Equation (4) for small perturbations around $(\mathbf{x}_0,\ \eta_0)$:

$$\dot{\mathbf{x}} = \dot{\mathbf{x}}_0 + \Delta\dot{\mathbf{x}} = \boldsymbol{\varphi}\ (\mathbf{x}, \eta) \tag{8}$$

From Equations (7) and (8), and considering $\dot{\mathbf{x}}_0 = \mathbf{f}(\mathbf{x}_0) + \mathbf{g}(\mathbf{x}_0)\eta$, $\boldsymbol{\Delta}\dot{\mathbf{x}}$ can be written such as:

$$\boldsymbol{\Delta}\dot{\mathbf{x}} = \left(\frac{\partial \mathbf{f}(\mathbf{x})}{\partial \mathbf{x}} + \frac{\partial \mathbf{g}(\mathbf{x})}{\partial \mathbf{x}}\eta\right)_{\mathbf{x}_0,\eta_0} \boldsymbol{\Delta}\mathbf{x} + \mathbf{g}(\mathbf{x})_{\mathbf{x}_0,\eta_0}\boldsymbol{\Delta}\eta \tag{9}$$

Making the following changes:

$$\mathbf{F}_{\mathbf{x}_0,\eta_0} = \left(\frac{\partial \mathbf{f}\ (\mathbf{x})}{\partial \mathbf{x}} + \frac{\partial \mathbf{g}\ (\mathbf{x})}{\partial \mathbf{x}}\eta\right)_{\mathbf{x}_0,\eta_0};\ \mathbf{G}_{\mathbf{x}_0,\eta_0} = \mathbf{g}(\mathbf{x})_{\mathbf{x}_0,\eta_0} \tag{10}$$

Equation (9) can be expressed in a simplified form:

$$\boldsymbol{\Delta}\dot{\mathbf{x}} = \mathbf{F}_{\mathbf{x}_0,\eta_0}\Delta\mathbf{x} + \mathbf{G}_{\mathbf{x}_0,\eta_0}\boldsymbol{\Delta}\eta \tag{11}$$

Recalling from Equation (2), $\boldsymbol{\Delta}\dot{y}$ may be computed as follows:

$$\Delta\dot{\mathbf{y}} = C\Delta\dot{\mathbf{x}} \tag{12}$$

Substituting $\Delta\dot{\mathbf{x}}$ from Equation (11) into Equation (12), we obtain:

$$\Delta\dot{\mathbf{y}} = \mathbf{C}\mathbf{F}_{\mathbf{x}_0,\eta_0}\boldsymbol{\Delta}\mathbf{x} + \mathbf{C}\mathbf{G}_{\mathbf{x}_0,\eta_0}\Delta\eta \tag{13}$$

From Equation (13), $\boldsymbol{\Delta}\eta$ may be obtained by inversion as follows:

$$\boldsymbol{\Delta}\eta = \left(\mathbf{C}\mathbf{G}_{\mathbf{x}_0,\eta_0}\right)^{-1}\left(\Delta\dot{y} - \mathbf{C}\mathbf{F}_{\mathbf{x}_0,\eta_0}\boldsymbol{\Delta}\mathbf{x}\right) \tag{14}$$

The control task consists of tracking a reference signal r. Consequently, the error dynamics e may be determined as follows:

$$e = r - y \tag{15.1}$$

$$\Rightarrow\ \dot{e} = \dot{r} - \dot{y} \tag{15.2}$$

where y is the output variable.

Taking $\dot{y} \approx \boldsymbol{\Delta}\dot{y}$ for small discrete time steps and recalling from Equation (15.2), for which $\dot{y} = \dot{r} - \dot{e}$, then $\boldsymbol{\Delta}\eta$ may be written as such:

$$\boldsymbol{\Delta}\eta = \left(\mathbf{C}\mathbf{G}_{\mathbf{x}_0,\eta_0}\right)^{-1}\left(\dot{r} + \nu - \mathbf{C}\mathbf{F}_{\mathbf{x_0},\eta_0}\Delta\mathbf{x}\right) \tag{16}$$

where ν is chosen so that the following relationship is fulfilled [3]:

$$\dot{e} = -\nu \tag{17}$$

Thus, the error can be stabilised by choosing a suitable form of ν.

Online parameter estimation

Finding analytical solutions of $\mathbf{F}_{\mathbf{x}_0,\eta_0}$ and $\mathbf{G}_{\mathbf{x}_0,\eta_0}$ given in Equation (10) can be tasking. Using real-time estimations, such as the RLS method, is an alternative. The goal is to approximate $\mathbf{F}_{\mathbf{x}_0,\eta_0}$ and $\mathbf{G}_{\mathbf{x}_0,\eta_0}$ based on local state observations. The RLS formulation can be found in Ref. [15]. This technique allows us to estimate the states and control variations based on their increments [16, 17].

Transforming Equation (13) into discrete times yields the following representation:

$$\boldsymbol{\Delta}y_{k+1} = \mathbf{C}\tilde{\mathbf{F}}_k\boldsymbol{\Delta}\mathbf{x}_k + \mathbf{C}\tilde{\mathbf{G}}_k\boldsymbol{\Delta}\eta_k \tag{18}$$

where $\tilde{\mathbf{F}}_k$ and $\tilde{\mathbf{G}}_k$ are discrete form of $\mathbf{F}_{\mathbf{x}_0,\eta_0}$ and $\mathbf{G}_{\mathbf{x}_0,\eta_0}$.

$\boldsymbol{\Delta}y_{k+1}$ corresponds to the output variation, and depends on the current states increment $\boldsymbol{\Delta}\mathbf{x}_k$ and input increment $\boldsymbol{\Delta}\eta_k$. $\tilde{\mathbf{F}}_k$ and $\tilde{\mathbf{G}}_k$ may then be replaced by their estimates $\hat{\mathbf{F}}_k$ and $\hat{\mathbf{G}}_k$ so that:

$$\boldsymbol{\Delta}\hat{y}_{k+1} = \mathbf{C}[\,\boldsymbol{\Delta}\mathbf{x}_k\ \boldsymbol{\Delta}\eta_k\,]\begin{bmatrix}\hat{\mathbf{F}}_k^T\\ \hat{\mathbf{G}}_k^T\end{bmatrix} \tag{19}$$

Let us consider the vector of the estimated parameter $\hat{\boldsymbol{\Theta}}_k = \begin{bmatrix}\hat{\mathbf{F}}_k^T\\ \hat{\mathbf{G}}_k^T\end{bmatrix}$ and the vector of past increments $\mathbf{X}_k = [\boldsymbol{\Delta}\mathbf{x}_k\ \Delta\eta_k]^T$. Then, from Equation (19), $\boldsymbol{\Delta}\hat{y}_{k+1}$ can be compacted as follows:

$$\boldsymbol{\Delta}\hat{y}_{k+1} = \mathbf{C}\mathbf{X}_k^T\hat{\boldsymbol{\Theta}}_k \tag{20}$$

The following defines the error matrix ϵ_k as:

$$\epsilon_k = \boldsymbol{\Delta}\mathbf{x}_k - \boldsymbol{\Delta}\hat{\mathbf{x}}_k \tag{21}$$

From Ref. [15], $\hat{\boldsymbol{\Theta}}_k$ can be numerically computed such as:

$$\hat{\boldsymbol{\Theta}}_k = \hat{\boldsymbol{\Theta}}_{k-1} + \frac{\mathbf{L}_{k-1}\mathbf{X}_k}{\kappa + \mathbf{X}_k^T\mathbf{L}_{k-1}\mathbf{X}_k}\epsilon_k \tag{22}$$

Algorithm 1 RLS algorithm and covariance matrix update

Initialise $\boldsymbol{\Theta}_0$, $\mathbf{L}_0$
Set κ and $\boldsymbol{\epsilon}_{treshold}$
Compute $\hat{\boldsymbol{\Theta}}_k$ using Eq. (22)
Compute $\boldsymbol{\Delta}\hat{y}_{k+1}$ using Eq. (20)
Compute $\boldsymbol{\epsilon}_k$ using Eq. (21)
Update $\mathbf{L}_k$
  if abs $(\boldsymbol{\epsilon}_k) \preceq \boldsymbol{\epsilon}_{treshold}$
  then $\mathbf{L}_k = 10^3\mathbf{I}$
  else compute $\mathbf{L}_k$ using Eq. (23)

where the covariance matrix $\mathbf{L}_k$ can be expressed as follows:

$$\mathbf{L}_k = \frac{1}{\kappa}\left(\mathbf{L}_{k-1} - \frac{\mathbf{L}_{k-1}\mathbf{X}_k\mathbf{X}_k^T\mathbf{L}_{k-1}}{\kappa + \mathbf{X}_k^T\mathbf{L}_{k-1}\mathbf{X}_k}\right) \tag{23}$$

$\hat{\boldsymbol{\Theta}}_k$ and $\mathbf{L}_k$ are obtained using the matrix inversion lemma [15]. $\hat{\mathbf{F}}_k$ and $\hat{\mathbf{G}}_k$ entirely depend on the state variations and control inputs. The initial parameters $\boldsymbol{\Theta}_0$, $\mathbf{L}_0$ and forgetting factor κ must be set beforehand.

Algorithm 1 presents the update of the covariance matrix $\mathbf{L}_k$. The covariance matrix is updated when the estimation error ϵ_k reaches a threshold value $\boldsymbol{\epsilon}_{treshold}$.

Proportional Integral Derivative (PID) controller

From Equation (14), the DI requires a linear feedback controller ν [3]. Its value should be chosen so that stability is ensured according to Lyapunov criteria detailed in the appendix. For this reason, a basic PID controller is sufficient and may be expressed in Laplace form such as [3]:

$$\nu = \left(K_P + \frac{K_I}{s} + K_D s\right) e \tag{24}$$

where K_P, K_I and K_D are the PID gains.

Neural network adaptive controller

Using the estimations in Equation (20) frequently results in prediction errors in real-world applications [24–26]. Including prediction errors ϵ_1 into (14), the input $\Delta\eta_k$ can be written as:

$$\Delta\eta_k = \left(\mathbf{C}\hat{\mathbf{G}}_k\right)^{-1}\left[\Delta y_{k+1} - \mathbf{C}\hat{\mathbf{F}}_k\boldsymbol{\Delta}\mathbf{x} - \epsilon_1\right] \tag{25}$$

From Equations (16) and (17), $\Delta\eta_k$ in Equation (25) can be written:

$$\boldsymbol{\Delta}\eta_k = \left(\mathbf{C}\hat{\mathbf{G}}_k\right)^{-1}\left[\dot{r} + \nu - \mathbf{C}\hat{\mathbf{F}}_k\boldsymbol{\Delta}\mathbf{x} - \epsilon_1\right] \tag{26}$$

The variables $\mathbf{C}\hat{\mathbf{G}}_k$ and $\mathbf{C}\hat{\mathbf{F}}_k\boldsymbol{\Delta}\mathbf{x}$ in Equation (26) represent the aircraft's local dynamics. To rectify the uncertainties and estimation errors for $\hat{\mathbf{F}}_k$ and $\hat{\mathbf{G}}_k$, the estimation error can be compensated with an adaptive term ν_{ad} so that:

$$\epsilon_1 = \nu_{ad} \tag{27}$$

An FFNN was used to train ν_{ad} as seen in Fig. 3(b).

The effectiveness of the FFNN in Fig. 3 is determined by its hyperparameters, including the number of neurons and hidden layers, the activation function $\boldsymbol{\sigma}$ and the weights $\mathbf{W}$ and $\mathbf{V}$. The output from the NN may be written such as [3]:

$$\hat{\nu}_{ad} = \mathbf{W}^{\mathbf{T}}\sigma(\mathbf{V}^{\mathbf{T}}\bar{\mathbf{x}}) \tag{28}$$

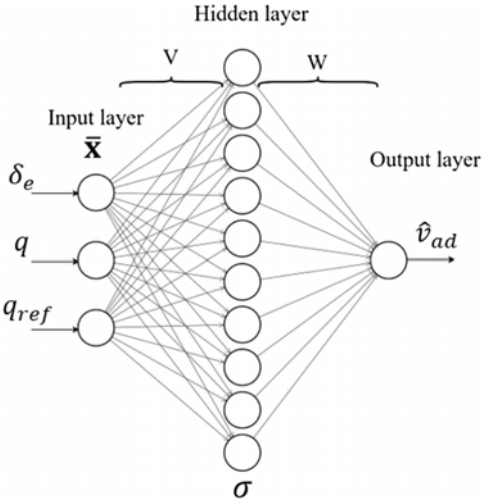

Figure 3. *Representation of a feedforward neural network.*

where $\sigma \in \mathbb{E}^{N\times N}$, with N – the number of neurons in the hidden layer, $\bar{\mathbf{x}} = [\delta_e\ q_{ref}\ q]^{\mathbf{T}}$, with $\bar{\mathbf{x}} \in \mathbb{E}^{m\times 1}$ denotingthe input vector, and $\mathbf{W} \in \mathbb{E}^{N\times n}$ and $\mathbf{V} \in \mathbb{E}^{m\times N}$, with n representing the number of network outputs. The activation function in the middle layer corresponds to a *tangent sigmoid* function such as:

$$\sigma_i(z) = \frac{1}{1+e^{-z}} \tag{29}$$

where i denotes the neuron's rank. An affine function was used in the input and output layers.

The adaptive signal $\hat{v}_{ad}$ is multiplied by a gain K_{NN}, which allows us to control the amplitude of the adaptive term $\hat{v}_{ad}$. Consequently:

$$v_{ad} = K_{NN}\hat{v}_{ad} = K_{NN}\mathbf{W}^T\sigma(\mathbf{V}^T\bar{\mathbf{x}}) \tag{30}$$

Adaptation laws

The following adaptation laws taken from the backpropagation principle [38–45, 47–52] are used to update the NN hyperparameters:

$$\begin{aligned}\dot{\mathbf{W}} &= -\left[\left(\boldsymbol{\sigma} - \sigma'\mathbf{V}^T\bar{\mathbf{x}}\right)e^T + \lambda\,\|e\|\,\mathbf{W}\right]\boldsymbol{\Gamma}_{\mathrm{W}} \\ \dot{\mathbf{V}} &= -\boldsymbol{\Gamma}_V\left[\bar{\mathbf{x}}e^T\mathbf{W}^T\boldsymbol{\sigma}' + \lambda\,\|e\|\,\mathbf{V}\right]\end{aligned} \tag{31}$$

where e is the tracking error, $\boldsymbol{\Gamma}_{\mathrm{W}}$ and $\boldsymbol{\Gamma}_{\mathbf{V}}$ are learning rate matrices, σ' is the derivative of σ, and λ is a scalar that is equal to 1. In Ref. [38], the additional terms $-\lambda\|e\|\mathbf{W}\boldsymbol{\Gamma}_{\mathrm{W}}$ and $-\lambda\,\|e\|\,\mathbf{V}\boldsymbol{\Gamma}_{\mathrm{V}}$. The adaptation law shown in Equation (31) ensures robustness and stability. A fixed learning rate $\boldsymbol{\Gamma}$ was considered for diagonal matrices $\boldsymbol{\Gamma}_{\mathrm{W}}$ and $\boldsymbol{\Gamma}_{\mathbf{V}}$ for the input and output weights, respectively. The backpropagation algorithm is considered as the *steepest descent* approximation when $\boldsymbol{\Gamma}$ is set to constant.

2.3 Control law

The overall control law may be obtained by substituting Equations (24), (27) and (30) into Equation (26), such that:

$$\boldsymbol{\Delta}\eta_k = \left(\mathbf{C}\hat{\mathbf{G}}_k\right)^{-1}\left[\dot{r} + \left(K_P + \frac{K_I}{s} + K_D s\right)e - \mathbf{C}\hat{\mathbf{F}}_k\boldsymbol{\Delta}\mathbf{x}_k - K_{NN}\mathbf{W}^T\sigma\left(\mathbf{V}^T\bar{\mathbf{x}}\right)\right] \tag{32}$$

Table 3. *Level 1 longitudinal flight quality requirements for category B cruise flights*

Parameters	Range
Short period frequency, rad/**s**	$0.3 \leq \omega_{\text{sp}} \leq 2$
Control anticipation parameter	$0.085 \leq \text{CAP} \leq 3.6$
Settling time at $\pm 5\%$, sec	$T_s < 3$
Dropback	$-0.2 \leq \frac{D_{rb}}{q_{ss}} \leq 0.5$
Short-period time constant, sec	$0.1 \leq T_{\theta_2} \leq 1.5$
Delay allowed, sec	0.1

2.4 Reference model

The proposed algorithm consists of a model reference adaptive controller and controls the pitch rate q, which is a primary state variable for *short period* motion. The *short period* and can be approximated by a second-order transfer function:

$$\frac{q_{ref}}{q_{cmd}} = \frac{\omega_{sp}^2 \left(1 + T_{\theta_2} s\right)}{s^2 + 2\xi_{sp}\omega_{sp} s + \omega_{sp}^2} \tag{33}$$

where s is the Laplace variable. The q_{ref} signal consists of the desired second order pitch rate signal, while q_{cmd} is a step input signal.

The design requirements for the damping ratio ξ_{sp} and natural frequency ω_{sp} are given by the flight qualities in MIL-STD-1797A [36]. Equation (33) is used to model the pitch rate reference model as depicted in Fig. 2. The zero of Equation (33) is defined as $-1/T_{\theta_2}$, where T_{θ_2} is the *short period* time constant.

2.5 Flight quality requirements

According to the MIL-STD 1797A [36], the Cessna Citation X can be categorised as a Class II aircraft. The proposed longitudinal controller was designed for Category B cruise operations. Table 3 establishes the Level 1 flight quality (FQ) requirements for *short period* dynamics.

2.6 Performance metrics

The overall sum squared error denoted as *overall SSE* was used for optimal tuning of the controller for a given number of flight conditions, so that:

$$overall\ SSE = \sum_{i=1}^{i=N} SSE_i \tag{34}$$

where N is the number of flight conditions.

The SSE for a single flight condition is computed as follows:

$$SSE = \sum_{t=0}^{t=T} (q_t - q_{ref_t})^2 \tag{35}$$

where q_t and q_{ref_t} correspond to the pitch rate and the pitch rate reference at a given time t, respectively, and T is the simulation time with a sample time $\mathbf{\Delta} t = 0.02$ sec.

3.0 Controller simulation for ideal conditions

3.1 Controller tuning parameters

The controller in Fig. 2 was tuned through sensitivity-based tuning. First, the aircraft is trimmed for all cruise conditions over the operating envelope, for given altitude h, calibrated airspeed CAS, mass m and

Table 4. *Design parameters for the pitch rate controller*

Control element	Parameters	Value
PID	K_P, K_I, K_D	-1, -1, -0.1
RLS inversion controller	κ, $\mathbf{L}_0$, $\hat{\mathbf{F}}_0$, $\hat{\mathbf{G}}_0$	1.015, $10^7\mathbf{I}_{5,5}$, $\mathbf{I}_{4,4}$, $-\mathbf{0.1}_{4,1}$
NN controller	K_{NN}, learning rate $\mathbf{\Gamma}$ hidden layers, neurons	20, 11, 30
Reference model	ξ_{sp}, $\omega_{sp}T_{\theta_2}$	0.69, 4 rad/s 0.35 sec

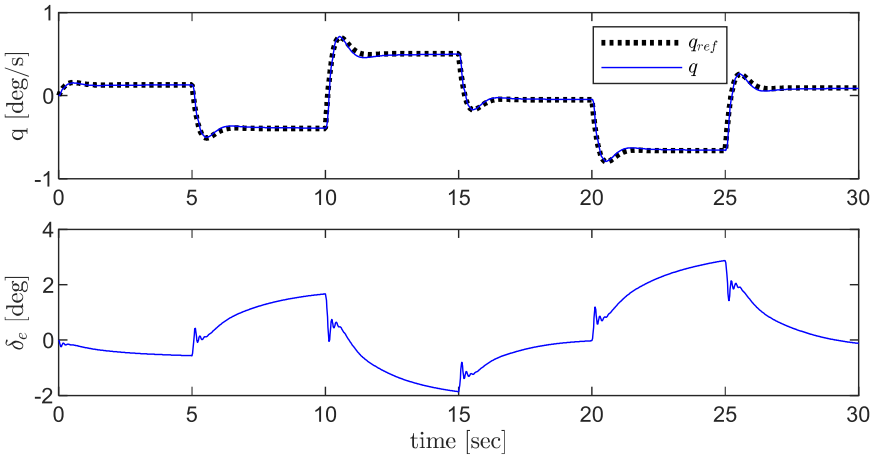

Figure 4. *Pitch rate and elevator responses for cruises at 35,000 ft and 290 kt.*

centre of gravity x_{cg}. Second, the PID gains K_P, K_I and K_D are tuned so that convergence is fulfilled. Third, the RLS inversion controller is tuned, for which the covariance matrix $\mathbf{L}_0$, the parameter vector $\mathbf{\Theta}_0$ and the forgetting factor κ are initialised. $\mathbf{L_k}$ is then iteratively updated following Algorithm 1. Then, the neural network learning rate $\mathbf{\Gamma}$ and gain K_{NN} are set. The NN weights are initialised from $\mathbf{0}$. Finally, robustness tests are performed. The control parameters are then adjusted throughout the process. The overall control parameter values are summed up in Table 4.

3.2 Simulation for cruise at 35,000 ft and 290 kn

Figure 4 shows the pitch rate control at 10,668 m [35,000 ft] and 537 km/h [290 kn]. The hyperparameter variations are shown in Fig. 5. Figure 6 shows the RLS parameters, including the covariance matrix $\mathbf{L}_k$ in Equation (23) and the prediction error ϵ_k in Equation (21). Figure 7 shows the RLS state estimations.

3.3 Simulation and validation over the flight envelope

3.3.1 Flight operating conditions

Sixty-four different cruise conditions were assessed to tune the controller. The aircraft was trimmed at given calibrated airspeeds (CAS) and altitudes. The flight conditions and flight envelope are shown in Fig. 8. A CoG of 25% and a weight of 15,000 kg [33,000 lb] were set for all simulations.

3.3.2 NN and RLS parameter sensitivity analysis

The effect of the NN and RLS parameters on the pitch rate reference tracking are shown in Figs. 9 and 10.

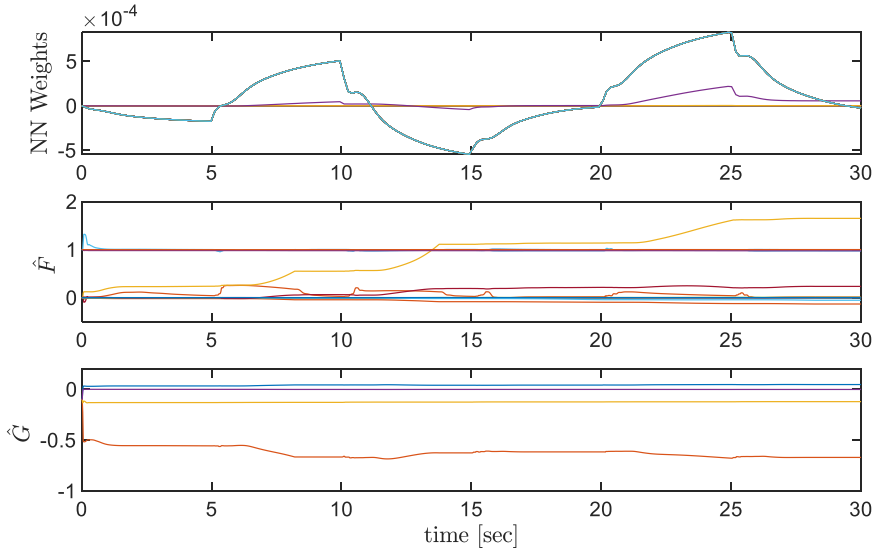

Figure 5. *Hyperparameter variation during cruise flight.*

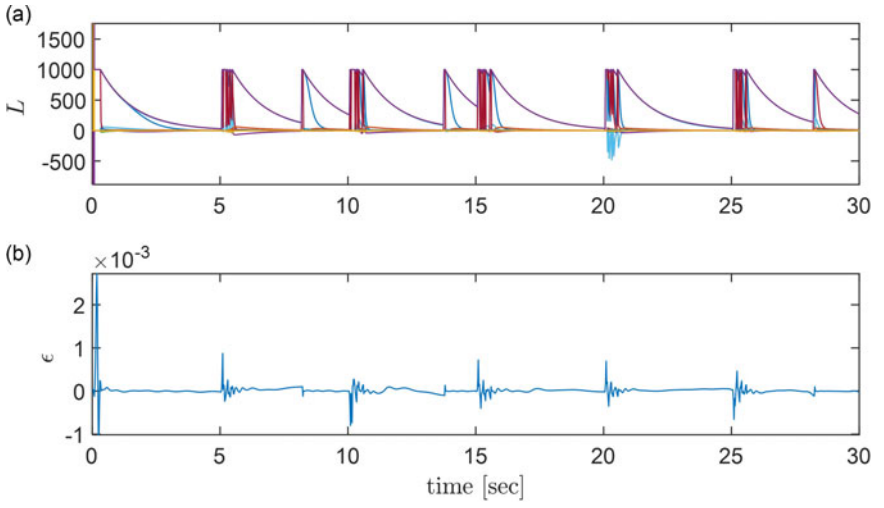

Figure 6. *(a) Covariance matrix* $\mathbf{L}_k$ *update and (b) prediction error during cruise.*

3.3.3 Controller tuning under wind gusts and turbulences

Figure 11 shows the *overall SSE* in Equation (34) for $N = 10$ flight conditions. The simulations in Fig. 11(b) include wind gusts with $u_{wind} = 40$ m/s [78 kn] and $w_{wind} = 5$ m/s [9.7 kn]. The cruise flights in Fig. 11(c) were simulated using the Dryden turbulence model [3] with moderate intensity. From Fig. 11(b) and Fig. 11(c), an optimal compromise of $\mathbf{\Gamma}$ and K_{NN} were found and summed up in Table 4.

3.4 Comparison of controller configurations

In Fig. 12, the tracking error is smaller when the adaptive controllers are successively added. This shows the contribution of each control element and the controller's ability to adapt across the flight envelope.

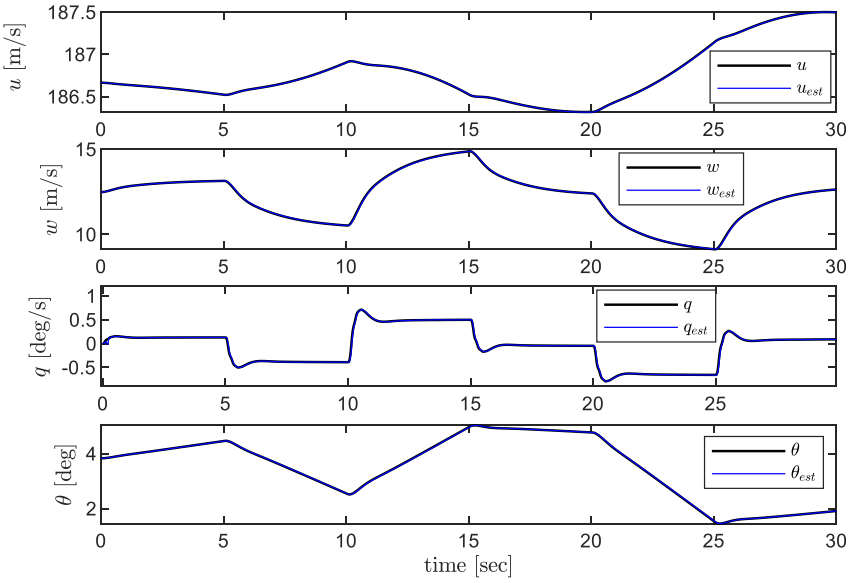

Figure 7. *Longitudinal states estimation using the RLS algorithm for cruise flight at 10,668 m AGL and 537 km/h.*

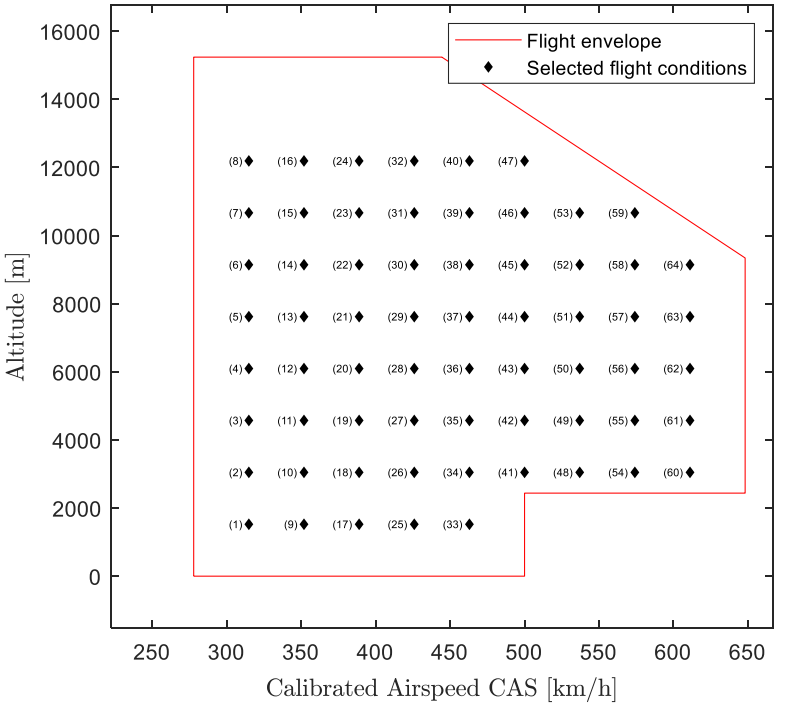

Figure 8. *Selected cruise conditions for $m = 15,000\,kg$ and CoG $x_{cg} = 25\%$ MAC.*

3.5 Flight quality validation

The pitch-rate controller was designed to satisfy the FQ requirements specified in MIL-STD-1797A for Class II, Category B aircraft. In this study, the reference model parameters (in Table 5) were selected to introduce a small overshoot of approximately 20% and steady state relative error below 1.2% in the

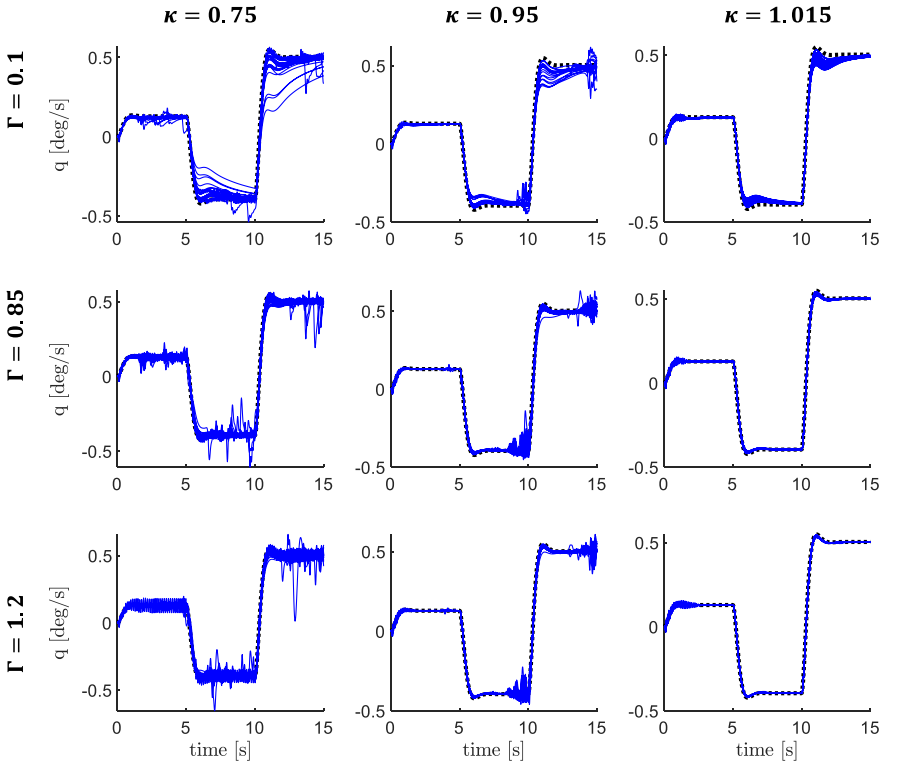

Figure 9. *Pitch rate response for different learning rates* $\mathbf{\Gamma}$ *and forgetting factors* κ *at all cruise conditions.*

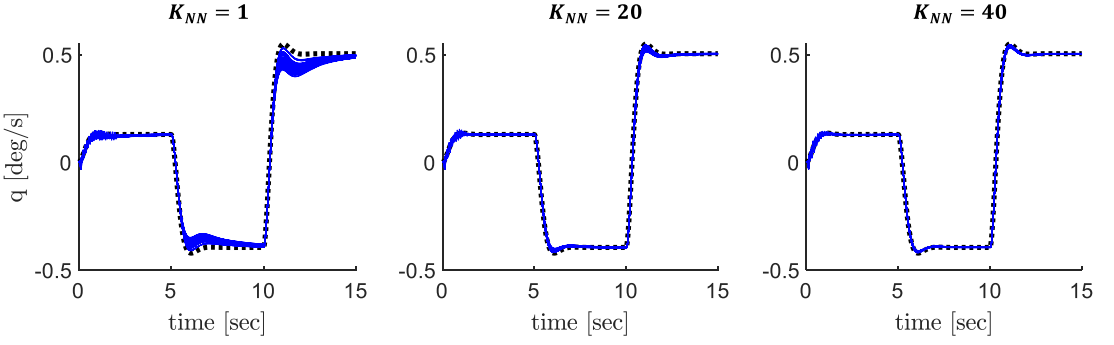

Figure 10. *Pitch rate response for three different neural networks gains* $\mathbf{K_{NN}}$ *values for all cruise conditions.*

pitch-rate response. This design choice was made to ensure compliance with the dropback requirement specified in Table 3 and defined in MIL-STD-1797A [36], rather than representing a formal Level 1 requirement. The FQ validation was carried out by assessing the short-period damping ratio ξ_{sp}, natural frequency ω_{sp}, and control anticipation parameter (CAP) across the flight envelope. As shown in Fig. 13, all identified short-period parameters and CAP values remained within Level 1 boundaries, confirming that the aircraft meets the required flying qualities. The controller's transient performances for all flight conditions are summarised in Table 6.

The aircraft flight qualities were assessed in Fig. 13(a) and Fig. 13(b). The dynamic parameters ξ_{sp}, ω_{sp} and T_{θ_2} in Equation (33) have been identified for each flight condition using system identification.

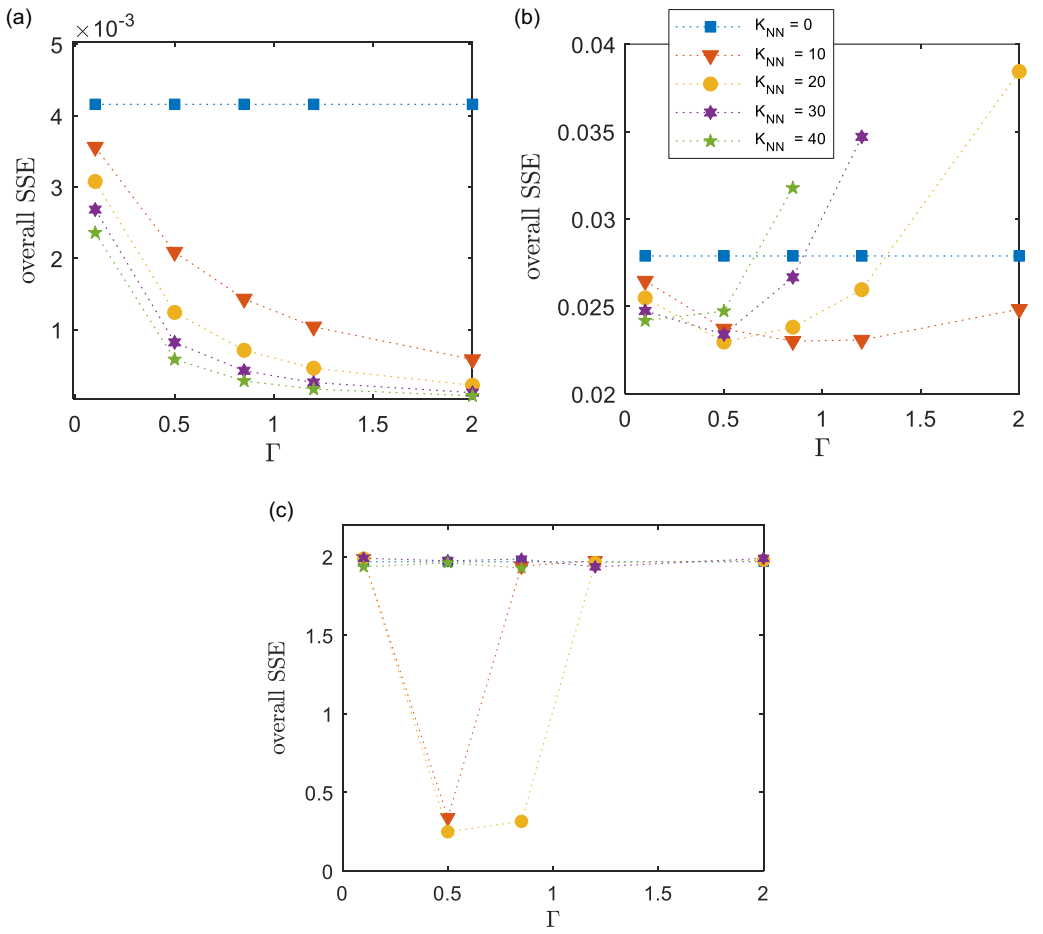

Figure 11. *Sum squared error contour plot for 10 flight conditions for (a) ideal conditions, (b) wind gust and (c) moderate turbulence.*

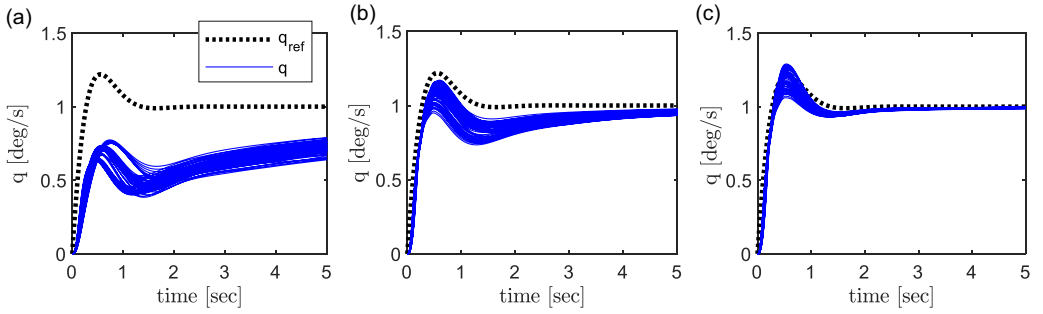

Figure 12. *Pitch rate response for different configurations for all cruise conditions: (a) PID controller, (b) PID – RLS Dynamic Inversion controller and (c) PID – RLS Dynamic Inversion – NN controller.*

For each flight condition, optimisation errors less than 2% were obtained, small enough to validate the identification. The CAP in Fig. 13(b) was also determined [37] and computed as follows:

$$CAP \approx \frac{\omega_{sp}^2}{\frac{V_0}{g}\frac{1}{T_{\theta_2}}}$$

Table 5. *Pitch rate reference model dynamic characteristics for level 1 flight quality*

Frequency, rad/s	Damping	Time constant, sec	Parameter	Dropback
ω_{sp}	ξ_{sp}	T_{θ_2}	$\omega_{sp}T_{\theta_2}$	$\frac{D_{rb}}{q_{ss}}$
4	0.69	0.5	2	0.155

Table 6. *Reference signal and pitch rate dynamic performance results*

Signal	Damping ξ_{sp}	Frequency, rad/s ω_{sp}	Rising time at 90%, sec T_r	Settling time at ±5% q_{ss}, sec T_s	Overshoot % –
Reference model q_{ref}	0.69	4	0.21	1.22	21
Pitch rate response	0.59–0.77	4.31–5.27	0.25–0.29	1–1.85	6–28

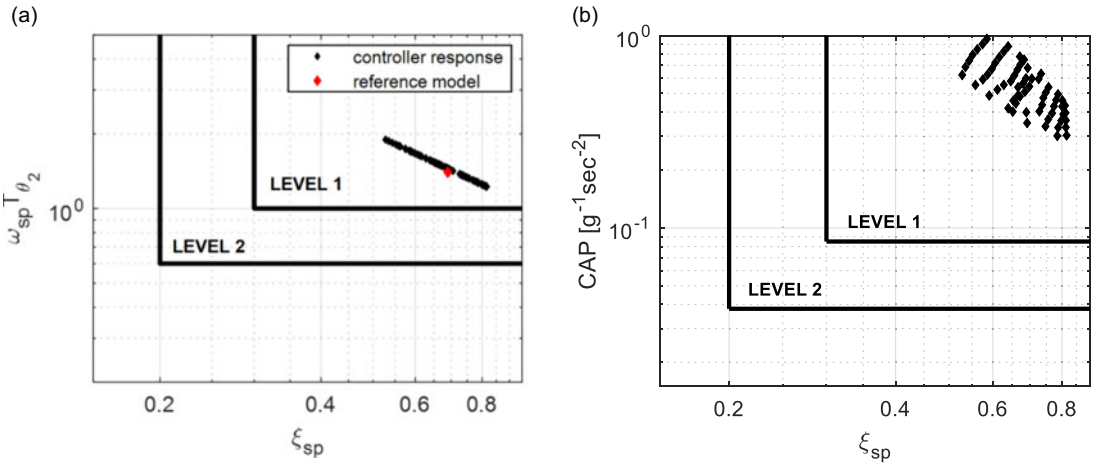

Figure 13. *Short period flight qualities for (a) damping and frequency requirements and (b) CAP requirements.*

where V_0 is the airspeed, g is the gravitational constant, equal to 9.81 m/**s**^{2} [32.18 ft/**s**^{2}], ω_{sp} is the short period frequency and T_{θ_2} is the short period time constant.

The Level 1 FQ boundaries given by MIL-STD-1797A [36] are depicted in Fig. 13(a) and 13(b). The FQ boundaries show the FAA requirements for optimal dynamic parameters ξ_{sp}, ω_{sp}, T_{θ_2} and CAP parameter. The pitch rate reference model dynamic parameters according to Table 6 are also represented. As seen in Fig. 13(a), the controller's dynamic parameters are close to the reference model and lying within the Level 1 region for all 64 flight conditions. This shows that the adaptive controller's dynamic performance is close to the targeted reference model and respects the FAA Level 1 criteria for the overall flight envelope. Furthermore, the CAP parameters for all flight conditions are also lying within the Level 1 region as seen in Fig. 13(b). The CAP parameters are gathered far from the Level 1 boundary, showing dynamic stability margin.

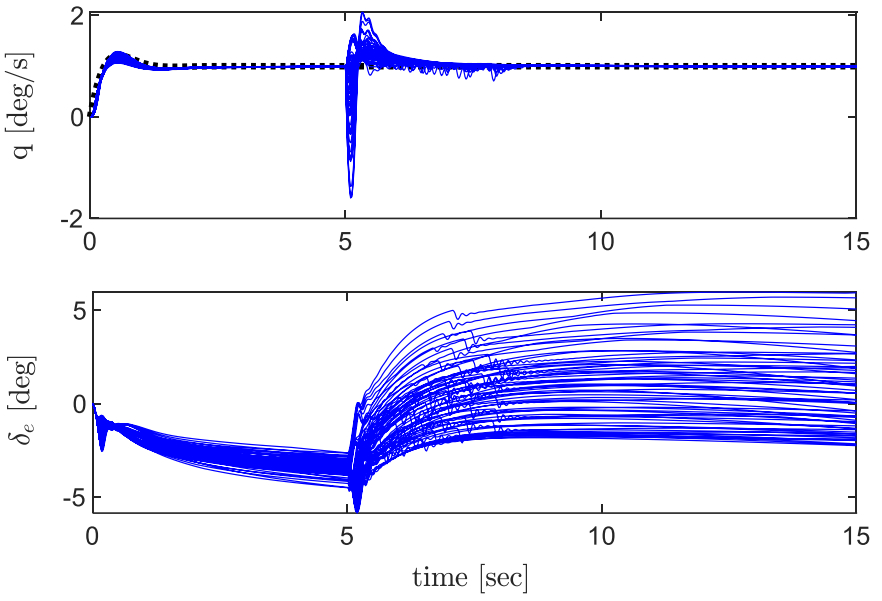

Figure 14. *Pitch rate and elevator responses under tailwind gust.*

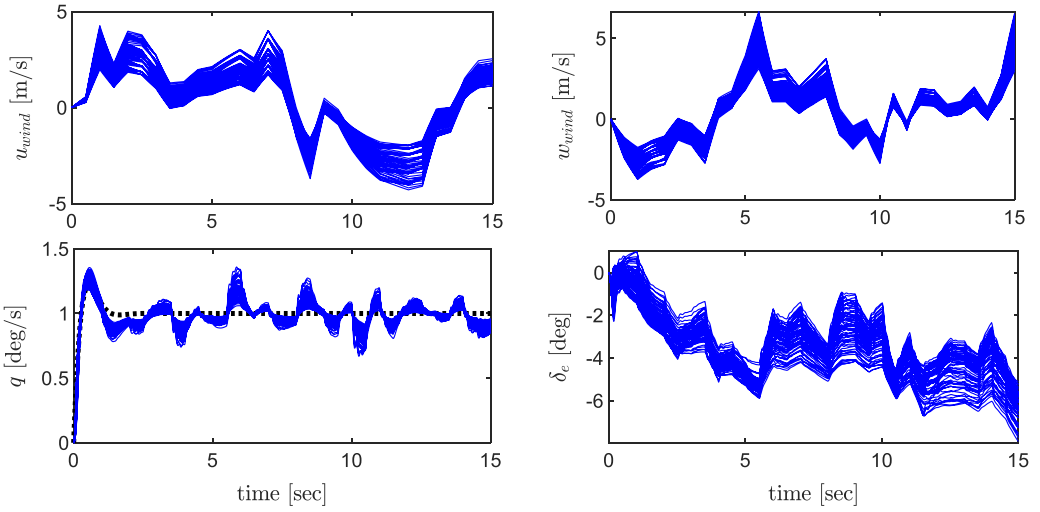

Figure 15. *Turbulence profiles at different altitudes, pitch rate and elevator responses.*

4.0 Robustness validation

4.1 Wind gust and turbulence tests

The controller was tested against wind gusts in Fig. 14 and turbulence in Fig. 15 [53].

The tailwind gust was simulated for $u_{wind} = 40$ m/s and $w_{wind} = 5$ m/s at $t = 5$ sec. The lateral wind component v_{wind} was set to 0 m/s. Figure 15 illustrates the controller's behaviour in the presence of turbulence. Dryden turbulence model was simulated for moderate turbulence in Simulink.

4.2 Actuator fault tests

Finally, the flight controller was validated for actuator faults [54]. Fifty per cent loss-of-effectiveness (LOE) on the elevators was simulated in Fig. 16(a), while white noises on the actuators are shown in Fig. 16(b). The actuator faults were added to the elevator's effectiveness $C_l^{\delta_e}$.

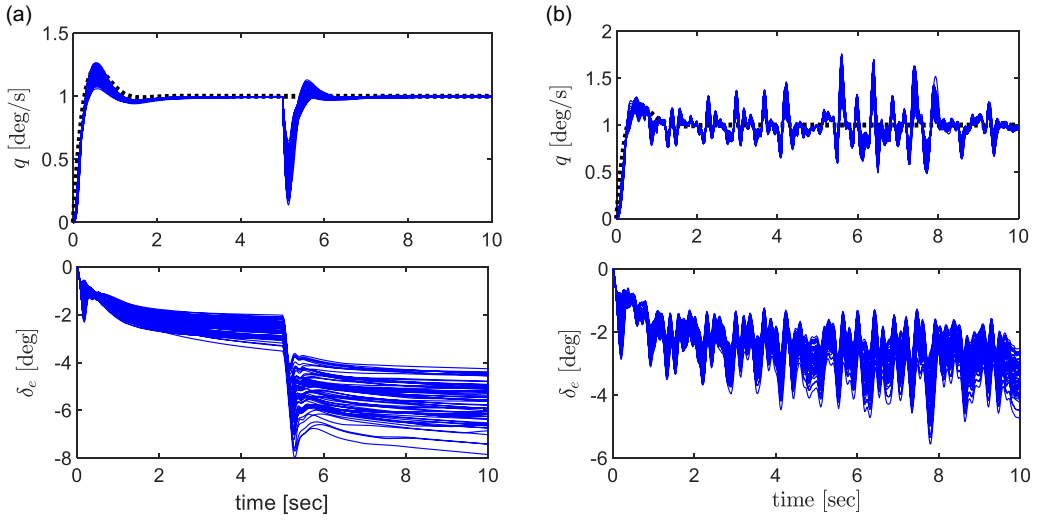

Figure 16. *Pitch rate, elevator and adaptive element responses for (a) 50% LOE and (b) actuator noise.*

5.0 Results and discussion

5.1 Controller performance

The proposed controller illustrated in Fig. 1 was first evaluated at a representative cruise condition of 10,668 m [35,000 ft] and CAS 537 km/h [290 kn]. As seen in Fig. 4, the pitch rate closely follows the reference command, with elevator deflections remain close to their trim values. Figure 5 shows the neural network weights and the RLS estimated matrices converged according to the adaptation laws in Equation (31) confirming the correct implementation of the online adaptation.

RLS updates were triggered when the prediction error exceeded a specified threshold, as shown in Fig. 6, preventing divergence and numerical instabilities. The estimated longitudinal states closely matched the measured states in Fig. 7, validating the RLS algorithm for online state identification.

A detailed parameter sensitivity study highlighted the complementary roles of the RLS-based dynamic inversion and the neural network. The RLS estimator was found to be highly sensitive to the forgetting factor κ: small values led to poor estimation due to rapid forgetting, while high values led to slower adaptation but more precise without oscillations. To mitigate these effects, the covariance matrix $\mathbf{L_k}$ was reinitialised when the prediction error exceeded a threshold, ensuring better estimation. As shown in Fig. 6(a), reinitialising $\mathbf{L_k}$ at $\mathbf{10^3 I_{5,5}}$ enabled fast convergence and precise estimation.

The neural network compensates for the RLS estimation errors. As demonstrated in Figs. 9 to 11, increasing the gain K_{NN} and the learning rate $\mathbf{\Gamma}$ reduced the overall SSE and improved adaptation under nominal conditions. However, overtuning these parameters may cause divergence in the presence of disturbances, as shown in Fig. 11(b) and Fig. 11(c). For instance, $K_{NN} = 10$ improved disturbance rejection but produced high SSE under ideal conditions, as seen in Fig. 11(a). This highlights the necessity of careful parameter tuning to achieve a balanced trade-off. Additional tests (Fig. 10) showed that higher NN gains improved short-term adaptation but also increased the risk of overtraining, making the controller overly sensitive to small variations.

The controller was then validated across 64 cruise conditions, for altitudes varying from 1,500 m [5,000 ft] to 12,200 [40,000 ft] and CAS from 314 km/h [170 kn] to 611 km/h [330 kn]. Sensitivity studies in Figs. 9 to 11 showed that higher values of the forgetting factor κ, NN learning rate Γ and NN gain K_{NN} improved adaptation but increased steady-state error under disturbances. Optimal parameters in Table 4 were selected in order to ensure compromise between tracking accuracy, robustness, stability and Level 1 FQ.

In Fig. 12, three configurations were compared: a baseline PID, a PID – RLS, and a PID – RLS – NN configuration. The full hybrid adaptive configuration (PID – RLS – NN) achieved the lowest tracking error and the strongest disturbance rejection, confirming the advantages of combining classic PID controllers with learning-based adaptation.

Flight quality assessment was conducted out using the reference model in Table 5, corresponding to Level 1 FQ. The reference model tracking produced smooth responses, with relative steady-state errors remaining below 0.1% within 1.9 seconds. As shown in Fig. 13, Level 1 flight qualities were consistently achieved for all flight conditions, as the short-period parameters and the CAP values remained within the required boundaries. Additional tests were performed in which the reference model was modified or removed, and Level 1 FQ were still maintained, demonstrating the controller's adaptability to different reference models. It is important to note that this study focuses on FQ validation using quantitative metrics defined in MIL-STD-1797A. A complete handling qualities (HQ) assessment requires pilot-in-the-loop evaluations with objective pilot rating criteria such as Gibson, Neal – Smith, or Bandwidth criteria. These HQ metrics are not included in the present work but may be addressed in future studies once pilot-in-the-loop simulation campaigns are conducted using the flight simulator shown in Fig. 1.

Finally, the robustness of the proposed controller was demonstrated under multiple uncertainties: wind gusts and Dryden turbulence of moderate intensity in Fig. 14 and actuator loss-of-effectiveness and actuator noise in Fig. 16. In all cases, the controller was able to maintain stability and to adapt the pitch rate within 1.9 sec settling time, while maintaining Level 1 FQ. The elevator deflections remained effective and unsaturated, even in the presence of uncertainties.

5.2 Comparative study

Across recent adaptive and intelligent flight control studies, different approaches have demonstrated notable improvements in tracking performance. Harris et al. [12] showed that L1 adaptive augmentation reduced manoeuvre tracking errors by 30–80%. This is also supported by the controller configuration comparative study, for which the PID – RLS – NN combination shows improved performance.

Steffensen et al. [10] established showed that their actuator-inclusive NDI achieved exact reference-model tracking with a 0.3 s settling time and 0% overshoot, while classical INDI exhibited residual error unless actuator bandwidths were effectively infinite. While their actuator model was limited to first-order dynamics, this paper focused on second order nonlinear actuator dynamics.

Andrianantara et al. [23] demonstrated that the model predictive controller – neural network controller for the Cessna Citation X allowed to reduce the steady-state error across its flight envelope, maintaining elevator deflections within ± 2 deg. In addition, this paper highlights the robustness of the adaptive controller with a single parameter set in Table 4 and analyses the control parameters sensitivity.

In the spacecraft control domain, Lungu et al. [32] showed that their adaptive NN – DI controller achieved convergence in less than 3 sec, with negligible steady-state error, and very low overshoot, outperforming conventional PID designs. In fighter aircraft applications, Pedro and Meyer [30] showed that their NN – DI controller predicted control deflections with high precision less than 0.05 deg for aileron, 1.5 deg for elevator and 0.5 deg for rudders, allowing safe landings with deviations limited to 1.5 m laterally and 4 m vertically, and thus in the presence of storm. Similarly, Lungu and Lungu [31] demonstrated that their NN – DI auto-landing controllers achieved altitude errors less than 0.5 m, velocity errors less than 0.3 m/s, and reduced overshoot in comparison with conventional landing control systems. Also, at the micro air vehicle scale, Zhou et al. [41] introduced extended INDI, which enabled oscillation-free optical-flow landings, reducing flow-divergence tracking RMSE to 0.10 s^{-1} versus 0.58 s^{-1} under conventional feedback, while adapting robustly across different initial heights and noisy environmental conditions. Nguyen et al. [22] demonstrated their hybrid NN – DI controller had a tracking error by over an order of magnitude compared to baseline control, achieving errors between 0.05 and 0.1 deg/s for pitch rate control and overshoot below 10%. Settling times were approximately 2–3 s under damaged aircraft scenarios such as tail loss or engine failure. While Nguyen's controller was validated under structural damage scenarios, it did not provide certification-relevant flight quality metrics.

By contrast, the hybrid PID – RLS – NN controller developed in this paper demonstrated its effectiveness in full-envelope longitudinal control of fixed-wing commercial aircraft such as the Cessna Citation X. It achieved steady-state pitch-rate errors below 0.1%, settling times under 1.9 secs, and overshoot between 6% and 28% across the flight envelope, all while maintaining Level 1 FQ. Unlike previous studies, robustness was explicitly validated under 40 m/s gusts, moderate Dryden turbulence, actuator loss-of-effectiveness and actuator noise, thereby confirming robustness performance under both environmental disturbances and system faults. While Harris et al. [12] and Lungu [32] controllers improved tracking error for specific cases, the proposed hybrid PID – RLS – NN controller achieved less than 0.1% steady-state errors and Level 1 FQ dynamics across the full operating envelope, with explicit robustness tests extending beyond ideal conditions or isolated scenarios.

6.0 Conclusion

An adaptive pitch-rate controller for the Cessna Citation X was developed and validated using a hybrid RLS- DI and a neural network adaptive controller. The design covered 64 cruise conditions, removing the need for gain scheduling, and achieved tracking with relative steady-state errors less than 0.1% in 1.9 sec.

Compared to classical PID-based methods, the proposed controller relies on a fixed-gain PID for baseline stability, while adaptive features ensure robustness against uncertainties and low tracking errors. Sensitivity analysis highlighted the critical influence of RLS initialisation and forgetting factor, as well as the importance of finding compromise between the neural network gain and learning rate. A covariance reinitialisation strategy was introduced to prevent numerical instabilities in the RLS, while the neural network compensated for estimation errors, enabling dual robust adaptation even under disturbances.

Flight quality evaluation confirmed Level 1 compliance across all tested scenarios, including turbulence, actuator faults and actuator noise. Lyapunov stability analysis further verified the convergence of all adaptive elements.

Overall, the results demonstrate that the proposed controller design provides a certifiable method to validate adaptive flight control in commercial aircraft by combining classic PID controllers with adaptive robust controllers, and validated flight qualities. Future work can be foreseen by extending the proposed hybrid adaptive controller to more general non-affine models to further enhance robustness and applicability to more complex nonlinearities.

Acknowledgements. This study was performed at the Laboratory of Applied Research in Active Controls, Avionics and AeroServoElasticity (LARCASE), in the framework of the CREATE UTILI programme, and the Canada Research Chairs funded by the Natural Sciences and Engineering Research Council of Canada (NSERC). The Cessna Citation X Research Flight Simulator (RAFS) was obtained by Dr. Ruxandra Botez, full professor, thanks to research grants approved by the Canadian Foundation of Innovation (CFI), and the Ministère du Développement Économique, de l'Innovation et de l'Exportation (MDEIE) and the contributions of CAE Inc.

References

[1] Federal Aviation Administration. *Human Factors Guide for Aviation Maintenance*, Federal Aviation Administration, 2009, Washington, DC.

[2] Wunderlich, T.F., Dähne, S., Reimer, L. and Schuster, A. Global aero-structural design optimization of composite wings with active manoeuvre load alleviation, *CEAS Aeronaut. J.*, 2022, **13**, pp 639–662.

[3] Stevens, B.L., Lewis, F.L. and Johnson, E.N. *Aircraft Control and Simulation: Dynamics, Controls Design, and Autonomous Systems*, John Wiley & Sons, Hoboken, NJ, 2015.

[4] Reynolds, O.R., Pachter, M. and Houpis, C. Full envelope flight control system design using quantitative feedback theory, *J. Guid. Control Dyn.*, 1996, **19**, pp 23–29.

[5] Khalil, A. and Fezans, N. Gust load alleviation for flexible aircraft using discrete-time preview control, *Aeronaut. J.*, 2021, **125**, pp 341–364.

[6] Efremov, A.V., Mbikayi, Z. and Efremov, E.V. Comparative study of different algorithms for a flight control system design and the potentiality of their integration with a sidestick, *Aerosp.*, 2021, **8**, pp 290.

[7] Ferrier, Y., Nguyen, N.T., Ting, E., Chaparro, D., Wang, X., de Visser, C.C. and Chu, Q.P. Active gust load alleviation of high-aspect ratio flexible wing aircraft, 2018 AIAA Guidance, Navigation, and Control Conference, 2018, p. 0620.

[8] Horn, J.F. Non-linear dynamic inversion control design for rotorcraft, *Aerosp.*, 2019, **6**, p 38.

[9] Moncayo, H., Perhinschi, M., Wilburn, B., Wilburn, J. and Karas, O. Extended nonlinear dynamic inversion control laws for unmanned air vehicles, AIAA Guidance, Navigation, and Control Conference, 2012, p 4675.
[10] Steffensen, R., Steinert, A. and Smeur, E.J. Nonlinear dynamic inversion with actuator dynamics: an incremental control perspective, *J. Guid. Control Dyn.*, 2022, **46**, pp 1–9.
[11] Doff-Sotta, M., Cannon, M. and Bacic, M., Data-driven robust model predictive control of tiltwing vertical takeoff and landing aircraft, *J. Guid. Control Dyn.*, 2025, **48**, pp 203–211.
[12] Harris, J., Elliott, C.M. and Tallant, G.S. L1 adaptive nonlinear dynamic inversion control for the innovative control effectors aircraft, AIAA SCITECH 2022 Forum, 2022, p. 0791.
[13] Kouvaritakis, B. and Cannon, M. *Model Predictive Control*, Springer International Publishing, 2016, Cham. doi: 10.1007/978-3-319-24853-0
[14] Eren, U., Prach, A., Koçer, B.B., Raković, S.V., Kayacan, E. and Açıkmeşe, B. Model predictive control in aerospace systems: current state and opportunities, *J. Guid. Control Dyn.*, 2017, **40**, pp 1541–1566. doi: 10.2514/1.G002507
[15] Haykin, S. *Adaptive Filter Theory: International Edition*, 5/E Pearson, Upper Saddle River, NJ, 2013.
[16] Mahadi, M., Ballal, T., Moinuddin, M. and Al-Saggaf, U.M. A recursive least-squares with a time-varying regularization parameter, *Appl. Sci.*, 2022, **12**, p 2077.
[17] Mohseni, N. and Bernstein, D.S. Recursive least squares with variable-rate forgetting based on the F-test, 2022 American Control Conference (ACC) IEEE, 2022, pp 3937–3942.
[18] Xiaoqian, T., Feicheng, Z., Zhengbing, T. and Hongying, W. Nonlinear extended Kalman filter for attitude estimation of the fixed-wing UAV, *Int. J. Optics*, 2022, **2022**, p 7883851.
[19] Konatala, R., Milz, D., Weiser, C., Looye, G. and van Kampen, E. Flight testing reinforcement-learning-based online adaptive flight control laws on CS-25-Class aircraft, *J. Guid. Control Dyn.*, 2024, **47**, pp 2460–2467.
[20] Andrianantara, R.P., Ghazi, G. and Botez, R.M. Neural network adaptive controller with approximate dynamic inversion for pitch control of the Cessna citation X, AIAA AVIATION 2023 Forum, 2023, p 3798.
[21] Quintin, E., Andrianantara, R.P., Ghazi, G. and Botez, R.M. Neural network adaptive controller with approximate dynamic inversion for the Cessna citation X lateral control, AIAA Scitech *2024 Forum*, 2024, p 0261.
[22] Nguyen, N. Hybrid adaptive flight control with model inversion adaptation, *Advances Flight Control Syst.*, 2011, **18**, p 19.
[23] Andrianantara, R.P., Ghazi, G. and Botez, R.M. Model predictive controller with adaptive neural networks and online state estimation for pitch rate control of the Cessna citation X, AIAA SCITECH 2024 Forum, 2024, p 0118.
[24] Ge, S.S., Hang, C.C., Lee, T.H. and Zhang, T. *Stable Adaptive Neural Network Control*, Springer Science & Business Media, Boston, MA, 2013.
[25] Liu, S., Lyu, W., Zhang, Q., Yang, C. and Whidborne, J.F. Neural-network-based incremental backstepping sliding mode control for flying-wing aircraft, *J. Guid. Control Dyn.*, 2025, **48**, pp 600–614.
[26] Emami, S.A., Castaldi, P. and Banazadeh, A. Neural network-based flight control systems: present and future, *Annu Rev. Control*, 2022, **53**, pp 97–137.
[27] Grigorie, T.L., Botez, R.M., Popov, A.V., Mamou, M. and Mébarki, Y. A hybrid fuzzy logic proportional- integral-derivative and conventional on-off controller for morphing wing actuation using shape memory alloy Part 1: morphing system mechanisms and controller architecture design, *Aeronaut. J.*, 2012, **116**, p 17.
[28] Hashemi, .S.M., Botez, R.M. and Grigorie, L.T. Adaptive fuzzy control of chaotic flapping relied upon Lyapunov-based tuning laws, AIAA Aviation 2020 Forum *(VIRTUAL EVENT: American Institute of Aeronautics and Astronautics)*, 2020. doi: 10.2514/6.2020-3193
[29] Hosseini, M.S., Ghazi, G. and Botez, R.M. New type-2-fuzzy-logic-based control system for the Cessna Citation X, *J. Aerosp. Inf. Syst.*, 2024, **21**, pp 846–864.
[30] Pedro, J. and Meyer, N. Neural network-based dynamic inversion controller for fighter aircrafts, *IFAC Proceedings Volumes*, 2007, **40**, pp 946–951.
[31] Lungu, M. and Lungu, R. Landing auto-pilots for aircraft motion in longitudinal plane using adaptive control laws based on neural networks and dynamic inversion, *Asian J. Control*, 2017, **19**, pp 302–315.
[32] Lungu, R., Lungu, M. and Efrim, C. Adaptive control of DGMSCMG using dynamic inversion and neural networks, *Adv. Space Res.*, 2021, **68**, pp 3478–3494.
[33] Park, O., Shin, H.-S., Lee, H.-I. and Antonios, T. Optimal and adaptive control design using recursive least square with a new exponential forgetting factor, *International Conference on Robot Intelligence Technology and Applications*, Springer, 2021, pp 116–128.
[34] Nguyen, N. and Krishnakumar, K. Hybrid damage adaptive flight control with model inversion adaptation, *IFAC Proceedings Volumes*, 2007, **40**, pp 657–662.
[35] Hakim, M. and Choukri, S. Froude similarity and flying qualities assessment in the design of a low-speed BWB UAV, *Int. J. Aeronaut. Space Sci.*, 2024, **25**, pp 46–60.
[36] Department of Defense. MIL-STD-1797A, Flying qualities of piloted aircraft, 1997.
[37] Hodgkinson, J. *Aircraft Handling Qualities*, American Institute of Aeronautics and Astronautics, 1999, Reston, VA.
[38] Narendra, K. and Annaswamy, A. A new adaptive law for robust adaptation without persistent excitation, *IEEE Trans. Autom. Control*, 1987, **32**, pp 134–145.
[39] Lewis, F.L., Yeşildirek, A. and Liu, K. Neural net robot controller: structure and stability proofs, *J. Intell. Rob. Syst.*, 1995, **12**, pp 277–299.
[40] O'Connell, M., Shi, G., Shi, X., Azizzadenesheli, K., Anandkumar, A., Yue, Y. and Chung, S.-J. Neural-fly enables rapid learning for agile flight in strong winds, *Sci. Rob.*, 2022, **7**, p eabm6597.

[41] Zhou, Y., Ho, H.W. and Chu, Q. Extended incremental nonlinear dynamic inversion for optical flow control of micro air vehicles, *Aerosp. Sci. Technol.*, 2021, **116**. p 106889.
[42] Federal Aviation Administration. *Roadmap for Artificial Intelligence Safety Assurance*, Federal Aviation Administration, 2024, Washington, DC.
[43] European Union Aviation Safety Agency. *Artificial Intelligence Concept Paper — Issue 2: Guidance for Level 1 & 2 Machine-Learning Applications*, EASA, 2024, Cologne, Germany.
[44] Agogino, A., Brat, G., He, Y., Hulse, D., Lipkis, R., Pressburger, T., Gopinath, D., Irshad, L., Katis, A., Mavridou, A. and others. Recommendations on evidence and process for certification of learning-enabled components in aerospace systems, 2024.
[45] Ghazi, G. and Botez, R. Development of a High-Fidelity Simulation Model for a Research Environment, 2015, pp 2015-01–2569. doi: 10.4271/2015-01-2569
[46] Hosseini, S., Inga, C., Ghazi, G. and Botez, R.M. Model-referenced adaptive flight controller based on recurrent neural network for the longitudinal motion of Cessna Citation X, AIAA AVIATION 2023 Forum, 2023, p 3797.
[47] Campbell, S., Nguyen, N., Kaneshige, J. and Krishnakumar, K. Parameter estimation for a hybrid adaptive flight controller, AIAA Infotech@ Aerospace Conference and AIAA Unmanned. . . Unlimited Conference, 2009, p 1803.
[48] Ghazi, G. and Botez, R.M. Lateral controller design for the Cessna Citation X with handling qualities and robustness requirements, *62nd CASI Aeronautics Conference and AGM,* (Montreal, Quebec, Canada, 2015).
[49] Boughari, Y., Botez, R.M., Ghazi, G. and Theel, F. Flight control clearance of the Cessna Citation X using evolutionary algorithms, *Proc. Inst. Mech. Eng. Part G: J. Aerospa. Engin.*, 2017, **231**, pp 510–532.
[50] Boughari, Y., Ghazi, G., Botez, R. M. and Theel, F. New methodology for optimal flight control using differential evolution algorithms applied on the cessna citation X business aircraft–Part 1, *Design and Optimization. INCAS Bulletin*, 2017, **9**, 31.
[51] Hosseini, S.M., Bematol, I., Ghazi, G. and Botez, R.M. Enhanced fuzzy-based super-twisting sliding-mode control system for the Cessna Citation X lateral motion, *Aerosp.*, 2024, **11**, 549.
[52] Kim, B.S. and Calise, A.J. Nonlinear flight control using neural networks, *J. Guid. Control Dyn.*, 1997, **20**, pp 26–33. doi: 10.2514/2.4029
[53] Gao, C. and Liu, H.H. Dubins path-based dynamic soaring trajectory planning and tracking control in a gradient wind field, *Optimal Control Appl. Methods*, 2017, **38**, pp 147–166.
[54] Hussein, M., Zhang, Y. and Liu, Z. Adaptive non-singular fast terminal sliding mode control for car-like vehicles with faded neighborhood information and actuator faults, *J. Intell. Rob. Syst.*, 2024, **110**, pp 1–14.
[55] Lavretsky, E. and Wise, K.A. Robust adaptive control, *Robust and Adaptive Control: With Aerospace Applications* (Springer, 2024), pp 469–506.

A. Appendix

The controller boundedness and convergence were assessed using Lyapunov criteria: for a given positive definite candidate $\mathcal{L}$, its derivative $\dot{\mathcal{L}}$ should be negative definite, such that [55]:

$$\mathcal{L} \geq 0 \quad \text{and} \quad \dot{\mathcal{L}} \leq 0 \tag{36}$$

Error dynamics

Let us consider the designed control law in Equation (32). Substituting $\dot{y}$ in Equation (15.2) by its expression in Equation (13), and applying the final control in Equation (32), it is easy to demonstrate that the error dynamic $\dot{e}$ may be defined as follows:

$$\dot{\mathbf{e}} = -\left(\mathbf{K_P} + \frac{\mathbf{K_I}}{\mathbf{s}} + \mathbf{K_D}\mathbf{s}\right)\mathrm{e} + \mathbf{K_{NN}}\mathbf{W^T}\boldsymbol{\sigma}(\mathbf{V^T}\bar{\mathbf{x}}) \tag{37}$$

Let us consider the optimal weights $\mathbf{V}$ as the sum of the current weights $\hat{\mathbf{V}}$ and optimisation error $\tilde{\mathbf{V}}$. The same logic applies to the output weight matrix $\mathbf{W}$, so that:

$$\mathbf{V} = \hat{\mathbf{V}} + \tilde{\mathbf{V}} \text{ and } \mathbf{W} = \hat{\mathbf{W}} + \tilde{\mathbf{W}} \tag{38}$$

where $\hat{\mathbf{W}}$ and $\hat{\mathbf{V}}$ are known values, and $\tilde{\mathbf{W}}$ and $\tilde{\mathbf{V}}$ are unknown errors. The optimal weights $\mathbf{W}$ and $\mathbf{V}$ are therefore unknown.

We can express the Taylor series approximation of the *tangent sigmoid* function $\sigma(\mathbf{V}^T\bar{\mathbf{x}})$ around the current argument $\hat{V}^T\bar{\mathbf{x}}$ as follows:

$$\boldsymbol{\sigma}\left(\mathbf{V^T}\bar{x}\right) = \boldsymbol{\sigma}\left(\hat{V}^{\mathbf{T}}\bar{x}\right) + \boldsymbol{\sigma}'\left(\hat{V}^{\mathbf{T}}\bar{x}\right)\tilde{\mathbf{V}}\bar{x} + \mathcal{O}^2\left(\tilde{\mathbf{V}}^{\mathbf{T}}\bar{x}\right) \tag{39}$$

where $\sigma'\left(\hat{V}^{\mathbf{T}}\bar{x}\right)$ is the gradient of $\sigma\left(\hat{V}^{\mathbf{T}}\bar{x}\right)$, and $\mathcal{O}^2\left(\tilde{V}^{\mathbf{T}}\bar{x}\right)$ is the unknown higher-order term.

For further calculations, let us consider the following notations:

$$\boldsymbol{\sigma}\left(\hat{V}^{\mathbf{T}}\bar{x}\right)=\hat{\boldsymbol{\sigma}} \text{ and } \boldsymbol{\sigma}'\left(\hat{V}^{\mathbf{T}}\bar{x}\right)=\hat{\sigma}' \tag{40}$$

where $\hat{\sigma}$ and $\hat{\sigma}'$ are known values.

By substituting Equations (38) and (39) into Equation (37), it is easy to obtain:

$$\dot{\mathbf{e}}= -\left(\mathbf{K_P}+\frac{\mathbf{K_I}}{\mathbf{s}}+\mathbf{K_D}\mathbf{s}\right)\mathrm{e}+\mathbf{K}_{\mathrm{NN}}\hat{W}^{\mathbf{T}}\hat{\sigma}+\mathbf{K}_{\mathrm{NN}}\tilde{W}^{\mathbf{T}}\hat{\sigma}+\mathbf{K}_{\mathrm{NN}}\mathrm{W}^{\mathbf{T}}\hat{\sigma}'\tilde{V}^{\mathbf{T}}\bar{x}+\mathbf{K}_{\mathrm{NN}}\mathrm{W}^{\mathbf{T}}\mathcal{O}^2\left(\tilde{V}^{\mathbf{T}}\bar{x}\right) \tag{41}$$

Linear components with respect to $\tilde{W}$ and $\tilde{V}$ can be easily approximated with suitable tuning of $\boldsymbol{\Gamma}$ [38, 39], while the terms containing two or more unknown parameters and higher-order terms constitute disturbances, so that Equation (41) can be written as:

$$\dot{\mathbf{e}}= -\left(\mathbf{K_P}+\frac{\mathbf{K_I}}{\mathbf{s}}+\mathbf{K_D}\mathbf{s}\right)\mathrm{e}+\mathbf{K}_{\mathrm{NN}}\hat{W}^{\mathbf{T}}\hat{\sigma}+\mathbf{K}_{\mathrm{NN}}\tilde{W}^{\mathbf{T}}\hat{\sigma}+\mathrm{d} \tag{42}$$

where d is the disturbance signal defined as

$$d=\mathbf{K}_{\mathrm{NN}}\mathrm{W}^{\mathbf{T}}\hat{\sigma}'\hat{V}^{\mathbf{T}}\bar{x}+\mathbf{K}_{\mathrm{NN}}\mathrm{W}^{\mathbf{T}}\mathcal{O}^2\left(\tilde{V}^{\mathbf{T}}\bar{\mathrm{x}}\right) \tag{43}$$

where $\mathbf{W}$, $\tilde{V}$ and $\mathcal{O}^2$ are unknown.

Disturbance boundedness

Through assumptions, Lewis et al. in Ref. [39] assessed the boundedness of d and demonstrated that d may be bounded as follows:

$$\|d\|\leq \mathrm{C}_0+\mathrm{C}_1\left\|\tilde{V}\right\|+\mathrm{C}_2\left\|\tilde{V}\right\|\|e\| \tag{44}$$

where C_0, C_1 and C_2 are computable positive constants.

Lyapunov candidate and its derivative

Let us assess the stability of the overall system. To achieve this, let us choose a positive definite Lyapunov candidate function $\mathcal{L}$ as follows:

$$\mathcal{L}=\frac{1}{2}\mathbf{e}\mathbf{e}+\frac{1}{2}\tilde{\boldsymbol{\Theta}}\mathbf{L}^{-1}\tilde{\boldsymbol{\Theta}}+\frac{1}{2}\tilde{\mathbf{W}}\boldsymbol{\Gamma}^{-1}\tilde{\mathbf{W}}+\frac{1}{2}\tilde{\mathbf{V}}\boldsymbol{\Gamma}^{-1}\tilde{\mathbf{V}} \tag{45}$$

where $\tilde{\boldsymbol{\Theta}}$ is the difference between the optimal RLS parameter vector $\boldsymbol{\Theta}^*$ and its estimate $\hat{\boldsymbol{\Theta}}$, such that:

$$\tilde{\boldsymbol{\Theta}}=\boldsymbol{\Theta}^*-\hat{\boldsymbol{\Theta}} \tag{46}$$

The Lyapunov candidate function in Equation (45) includes all the controller adaptive parameters. Its derivative may be written as follows:

$$\dot{\mathcal{L}}=\dot{\mathbf{e}}\mathbf{e}+\dot{\tilde{\boldsymbol{\Theta}}}\mathbf{L}^{-1}\tilde{\boldsymbol{\Theta}}+\dot{\tilde{\mathbf{W}}}\boldsymbol{\Gamma}^{-1}\tilde{\mathbf{W}}+\dot{\tilde{\mathbf{V}}}\boldsymbol{\Gamma}^{-1}\tilde{\mathbf{V}} \tag{47}$$

RLS controller stability

Here we assess the second term of Equation (45) and demonstrate its negative definiteness.

$$\mathcal{L}_2=\frac{1}{2}\tilde{\boldsymbol{\Theta}}\mathbf{L}^{-1}\tilde{\boldsymbol{\Theta}} \tag{48}$$

Its derivative may be computed as follows:

$$\dot{\mathcal{L}}_2=\tilde{\boldsymbol{\Theta}}\mathbf{L}^{-1}\dot{\tilde{\boldsymbol{\Theta}}} \tag{49}$$

where $\mathbf{L}^{-1}$ is the inverse covariance matrix.

Let us express $\tilde{\boldsymbol{\Theta}}$ in discrete time at $k-1$ and k, so that:

$$\begin{aligned}\tilde{\boldsymbol{\Theta}}_{\mathbf{K}-1} &= \Theta^* - \hat{\boldsymbol{\Theta}}_{\mathbf{K}-1} \\ \tilde{\boldsymbol{\Theta}}_{\mathbf{K}} &= \Theta^* - \hat{\boldsymbol{\Theta}}_{\mathbf{K}}\end{aligned} \tag{50}$$

From Equation (22), $\hat{\boldsymbol{\Theta}}_k$ can be written as:

$$\hat{\boldsymbol{\Theta}}_{\mathbf{K}} = \hat{\boldsymbol{\Theta}}_{\mathbf{K}-1} + \mathbf{K}_{\mathbf{K}}\epsilon_{\mathbf{K}} \tag{51}$$

where K_k is the Kalman gain vector defined as:

$$\mathbf{K}_{\mathbf{k}} = \frac{\mathbf{L}_{\mathbf{k}-1}\mathbf{X}_{\mathbf{k}}}{\kappa + \mathbf{X}_{\mathbf{k}}^{\mathbf{T}}\mathbf{L}_{\mathbf{k}-1}\mathbf{X}_{\mathbf{k}}} \tag{52}$$

Taking into account Equation (51), $\dot{\tilde{\boldsymbol{\Theta}}}$can be expressed as:

$$\dot{\tilde{\boldsymbol{\Theta}}} = \tilde{\boldsymbol{\Theta}}_{\mathbf{k}} - \tilde{\boldsymbol{\Theta}}_{\mathbf{k}-1} = -\mathbf{K}_{\mathbf{k}}\boldsymbol{\epsilon}_{\mathbf{k}} \tag{53}$$

Therefore, substituting Equation (25) into (49), the derivative $\dot{\mathcal{L}}_2$ can be expressed as:

$$\dot{\mathcal{L}}_2 = -\tilde{\boldsymbol{\Theta}}\mathbf{L}^{-1}\mathbf{K}_{\mathbf{k}}\boldsymbol{\epsilon}_{\mathbf{k}} \tag{54}$$

Let us assess the definiteness of Equation (54). The elements of $\tilde{\boldsymbol{\Theta}}$ can be positive or negative, depending on whether $\hat{\boldsymbol{\Theta}}_k$ are underestimating or overestimating $\boldsymbol{\Theta}^*$. The magnitude of $\tilde{\boldsymbol{\Theta}}$ is expected to decrease over time, tending to zero as $\hat{\boldsymbol{\Theta}}_k$ converges to $\boldsymbol{\Theta}^*$. Consequently, the magnitude of the estimation error ϵ_k decreases. The sign of ϵ_k may still vary; however, these variations become smaller and less frequent, since the estimates $\hat{\boldsymbol{\Theta}}_k$ are stabilising.

The sign of the Kalman gain vector $\boldsymbol{K_k}$ in the context of the Recursive Least Squares algorithm is generally positive. However, it is more accurate to say that $\boldsymbol{K_k}$ is a vector that scales the correction applied to the parameter estimates rather than focusing solely on its sign, as shown in Equation (51).

The inverse covariance matrix $\mathbf{L}^{-1}$ is positive definite; therefore, the definiteness of Equation (54) relies on K_k, ϵ_k and $\tilde{\boldsymbol{\Theta}}$. The Kalman gain vector K_k is chosen to minimise the estimation error ϵ_k and the optimisation error $\tilde{\boldsymbol{\Theta}}$. Therefore, in order to guarantee that $\mathcal{L}_2$ decreases over time, we typically aim for K_k to be chosen such that the product $K_k\epsilon_k$ aligns with the direction of $\tilde{\boldsymbol{\Theta}}$, leading to a positive value. This positive dot product indicates that $\dot{\mathcal{L}}_2$ is negative definite, and that $\mathcal{L}_2$ in Equation (48) is monotonically decreasing. In that case, the stability and convergence of the RLS algorithm are verified.

Boundedness and convergence

Let us consider the derivative of the Lyapunov candidate in Equation (47), and demonstrate its boundedness.

$$\dot{\mathcal{L}} = \dot{\mathbf{e}}\mathbf{e} + \dot{\tilde{\boldsymbol{\Theta}}}\mathbf{L}^{-1}\tilde{\boldsymbol{\Theta}} + \dot{\tilde{W}}\boldsymbol{\Gamma}^{-1}\tilde{W} + \dot{\tilde{V}}\boldsymbol{\Gamma}^{-1}\tilde{V} \tag{55}$$

where $\mathbf{V}$ and $\mathbf{W}$ are the neural network input and output weight matrices, respectively, $\dot{\mathbf{V}}$ and $\dot{\mathbf{W}}$ are their respective time derivatives and, $\boldsymbol{\Gamma}^{-1}$ is the inverse learning rate diagonal matrix.

Substituting $\dot{e}$, $\dot{\mathbf{W}}$ and $\dot{\mathbf{V}}$ from their expressions in Equations (41) and (31) into Equation (55), we obtain:

Considering the assumptions in Equation (38) and making all simplifications, Equation (55) can be simplified as:

$$\begin{aligned}\dot{\mathcal{L}} = -\mathrm{e}\left(\mathrm{K_P} + \frac{\mathrm{K_I}}{\mathbf{s}} + \mathrm{K_D}\mathbf{s}\right)\mathrm{e} + \hat{W}^{\mathbf{T}}\hat{\sigma}\mathrm{e} + \tilde{W}^{\mathbf{T}}\hat{\sigma}'\mathbf{V}^{\mathbf{T}}\bar{x}\mathrm{e} + \mathrm{W}^{\mathbf{T}}\mathcal{O}^2\left(\tilde{V}^{\mathbf{T}}\bar{x}\right)\mathrm{e} \\ + \dot{\tilde{\boldsymbol{\Theta}}}\mathbf{L}^{-1}\tilde{\boldsymbol{\Theta}} - \tilde{W}\lambda\,\|\mathrm{e}\|\,\hat{W} - \tilde{V}\lambda\,\|\mathrm{e}\|\,\hat{\mathbf{V}}\end{aligned} \tag{56}$$

where the gradient estimate $\hat{\boldsymbol{\sigma}}$ is assumed to be known.

Next, we assess the boundedness of each term of Equation (56). Following the reasoning in Ref. [39] and taking into account the assumption in Equation (38), the term $\hat{W}^T\hat{\sigma}e$ may be bounded as:

$$\left\|\hat{\mathbf{W}}^{\mathbf{T}}\hat{\sigma}e\right\| \leq \mathrm{W_m c_{11}}\|\mathrm{e}\| - \left\|\tilde{\mathbf{W}}\right\|\mathrm{c_{11}}\|\mathrm{e}\| \tag{57}$$

Following the reasoning in Ref. [39], it can be demonstrated that $\mathbf{W}^T\mathcal{O}^2\left(\tilde{V}^T\bar{x}\right)e$ may be bounded as follows:

$$\left\|\mathbf{W}^{\mathbf{T}}\mathcal{O}^2\left(\tilde{\mathbf{V}}^{\mathbf{T}}\bar{\mathbf{x}}\right)\mathrm{e}\right\| \leq \mathrm{W_m c_3}\,\|\mathrm{e}\| + \mathrm{W_m c_{11} c_1 Q_d}\left\|\tilde{\mathbf{V}}\right\|\,\|\mathrm{e}\| + \mathrm{W_m c_{11} c_2}\left\|\tilde{\mathbf{V}}\right\|\|\mathrm{e}\|^2 \tag{58}$$

Next, the term $\tilde{W}^T\hat{\sigma}'\mathbf{V}\bar{\mathbf{x}}\mathbf{e}^{\mathbf{T}}$ in Equation (56) may be bounded as follows:

$$\left\|\tilde{\mathbf{W}}^T\hat{\sigma}'\mathbf{V}\bar{x}e^{\mathbf{T}}\right\| \leq V_m c_1 c_{11} Q_d\left\|\tilde{\mathbf{W}}\right\|\,\|e\| + V_m c_2 c_{11}\left\|\tilde{\mathbf{W}}\right\|\|e\|^2 \tag{59}$$

The term $\left(\tilde{\mathbf{W}}\left(\mathbf{W}-\tilde{\mathbf{W}}\right)+\tilde{\mathbf{V}}\left(\mathbf{V}-\tilde{\mathbf{V}}\right)\right)$ in Equation (56) may also be bounded as:

$$\left\|\lambda\|\mathrm{e}\|\left(\tilde{\mathbf{W}}\left(\mathbf{W}-\tilde{\mathbf{W}}\right)+\tilde{\mathbf{V}}\left(\mathbf{V}-\tilde{\mathbf{V}}\right)\right)\right\| \leq -\lambda\|\mathrm{e}\|\left(-\left\|\tilde{\mathbf{W}}\right\|^2 + W_m\left\|\tilde{\mathbf{W}}\right\| - \left\|\tilde{\mathbf{V}}\right\|^2 + \mathbf{V}_m\left\|\tilde{\mathbf{V}}\right\|\right) \tag{60}$$

It has been demonstrated that $\dot{\mathcal{L}}_2$ in Equation (54) is negative definite if the Kalman gain matrix K_k is chosen properly. However, even in the case where $\dot{\mathcal{L}}_2$ in Equation (54) is not negative definite, if the estimation is performed correctly, Equation (54) is ensured to converge to 0, as the errors ϵ_k and $\tilde{\mathbf{\Theta}}$ tend to zero over time. Therefore, the norm of $\dot{\mathcal{L}}_2$ in Equation (54) is monotonically decreasing to 0 and can therefore be neglected when accounting $\dot{\mathcal{L}}$ for boundedness.

The bound on $\dot{\mathcal{L}}$ can thus be stated as follows:

$$\begin{aligned}\dot{\mathcal{L}} \leq & -\left(\mathbf{K_P} + \frac{\mathbf{K_I}}{\mathbf{s}} + \mathbf{K_D s}\right)\|\mathrm{e}\|^2 \\ & + \mathrm{W_m c_{11}}\,\|\mathrm{e}\| - \left\|\tilde{W}\right\|\mathrm{c_{11}}\,\|\mathrm{e}\| + \mathbf{V_m c_1 c_{11} Q_d}\left\|\tilde{W}\right\|\,\|\mathrm{e}\| \\ & + \mathbf{V_m c_2 c_{11}}\left\|\tilde{W}\right\|\|\mathrm{e}\|^2 + \mathrm{W_m c_3}\,\|\mathrm{e}\| + \mathrm{W_m c_{11} c_1 Q_d}\left\|\tilde{V}\right\|\,\|\mathrm{e}\| \\ & + \mathrm{W_m c_{11} c_2}\left\|\tilde{V}\right\|\|\mathrm{e}\|^2 - \lambda\,\|\mathrm{e}\|\left(-\left\|\tilde{W}\right\|^2 + \mathrm{W_m}\left\|\tilde{W}\right\| - \left\|\tilde{V}\right\|^2 + \mathbf{V_m}\left\|\tilde{V}\right\|\right)\end{aligned} \tag{61}$$

For stability and convergence, the Lyapunov theory states that $\dot{\mathcal{L}}$ must be negative definite, as stated in Equation (36). On one hand, $\dot{\mathcal{L}} = 0$ when $\|\mathrm{e}\| = 0$, while on the other hand, Equation (36) is true when the following equation is true.

$$\begin{aligned}&\left(-\left(\mathbf{K_P} + \frac{\mathbf{K_I}}{\mathbf{s}} + \mathbf{K_D s}\right) + \mathbf{V_m c_2 c_{11}}\left\|\tilde{\mathbf{W}}\right\| + \mathrm{W_m c_{11} c_2}\left\|\tilde{\mathbf{V}}\right\|\right)\|\mathrm{e}\| + \mathrm{W_m c_{11}} - \left\|\tilde{\mathbf{W}}\right\|\mathrm{c_{11}} + \mathbf{V_m c_1 c_{11} Q_d}\left\|\tilde{\mathbf{W}}\right\| \\ &+ \mathrm{W_m c_3} + \mathrm{W_m c_{11} c_1 Q_d}\left\|\tilde{\mathbf{V}}\right\| - \lambda\left(-\left\|\tilde{\mathbf{W}}\right\|^2 + \mathrm{W_m}\left\|\tilde{\mathbf{W}}\right\| - \left\|\tilde{\mathbf{V}}\right\|^2 + \mathbf{V_m}\left\|\tilde{\mathbf{V}}\right\|\right) \leq 0\end{aligned} \tag{62}$$

Case 1

The NN approximation is performed properly, so $\|\tilde{\mathbf{W}}\|$and $\|\tilde{\mathbf{V}}\|$ are small and tend to 0. The term $-\lambda\left(-\left\|\tilde{\mathbf{W}}\right\|^2 + W_m\left\|\tilde{\mathbf{W}}\right\| - \left\|\tilde{\mathbf{V}}\right\|^2 + V_m\left\|\tilde{\mathbf{V}}\right\|\right)$ still remains negative definite, as W_m and V_m are higher values. Equation (62) can then be simplified as follows:

$$-\left(\mathbf{K_P} + \frac{\mathbf{K_I}}{\mathbf{s}} + \mathbf{K_D s}\right)\|\mathrm{e}\| + (\mathrm{W_m c_{11}} + \mathrm{W_m c_3}) \leq 0 \tag{63}$$

and an upper bound on the tracking error $\|\mathrm{e}\|$ may be found, such that:

$$\|\mathrm{e}\| \leq \frac{\mathrm{W_m c_{11}} + \mathrm{W_m c_3}}{\mathbf{K_P} + \frac{\mathbf{K_I}}{\mathbf{s}} + \mathbf{K_D s}} \tag{64}$$

Equation (64) clearly shows that the upper bound on the tracking error depends on the PID gains K_P, K_I and K_D. For the norm $\|e\|$ to remain positive and small, and thus, the negative definiteness of Equation (61) is ensured if the magnitudes of K_P, K_I and K_D are chosen high enough.

Case 2

In the case where the neural network approximation is performed poorly, then $\|\tilde{\mathbf{W}}\|$ and $\|\tilde{\mathbf{V}}\|$ are large. The term $-\lambda\left(-\|\tilde{\mathbf{W}}\|^2 + W_m\|\tilde{\mathbf{W}}\| - \|\tilde{\mathbf{V}}\|^2 + V_m\|\tilde{\mathbf{V}}\|\right)$ will still remain negative definite, as W_m and V_m are higher positive values. If $\|e\|$ is negligible, then Equation (36.2) remains true. On the contrary, if $\|e\|$ is large, then a proper choice of the linear PID controller gains would still ensure that Equation (36.2) remains true.

In sum, the PID gains ensure ultimate stability, while the neural network ensures negative definiteness. Furthermore, the term $\dot{\tilde{\mathbf{\Theta}}}\mathbf{L}^{-1}\tilde{\mathbf{\Theta}}$ in Equation (56) is small and converges to 0. In fact, if the amplitudes of K_P, K_I and K_D are chosen to be large enough, then the negative definiteness in Equation (36.2) is respected. In sum, in both cases, the overall system stability and convergence of the proposed controller are guaranteed.

Cite this article: Andrianantara R. P., Ghazi G. and Botez R. M. Nonlinear adaptive longitudinal controller and flight qualities validation for a business aircraft. *The Aeronautical Journal*, https://doi.org/10.1017/aer.2026.10132